ABSTRACT

Title of Thesis: FREQUENCY DOMAIN CHARACTERIZATION OF OPTIC FLOW AND VISION-BASED OCELLAR SENSING FOR ROTATIONAL MOTION

Nil Zeynep Gurel, Master of Science, 2016

Thesis Directed By: Associate Professor Timothy K. Horiuchi
Department of Electrical and Computer Engineering

The structure of an animal's eye is determined by the tasks it must perform. While vertebrates rely on their two eyes for all visual functions, insects have evolved a wide range of specialized visual organs to support behaviors such as prey capture, predator evasion, mate pursuit, flight stabilization, and navigation. Compound eyes and ocelli constitute the vision forming and sensing mechanisms of some flying insects. They provide signals useful for flight stabilization and navigation. In contrast to the well-studied compound eye, the ocelli, seen as the second visual system, sense fast luminance changes and allows for fast visual processing. Using a luminance-based sensor that mimics the insect ocelli and a camera-based motion detection system, frequency-domain characterization of an ocellar sensor and optic flow (due to rotational motion) are analyzed. Inspired by the insect neurons that make use of signals from both vision sensing mechanisms, complementary properties of ocellar and optic flow estimates are discussed.

FREQUENCY DOMAIN CHARACTERIZATION OF OPTIC FLOW AND VISION-BASED OCELLAR SENSING FOR ROTATIONAL MOTION

by

Nil Zeynep Gurel

Thesis submitted to the Faculty of the Graduate School of the
University of Maryland, College Park, in partial fulfillment
of the requirements for the degree of
Master of Science
2016

Advisory Committee:
Professor Timothy K. Horiuchi, Chair
Professor Robert W. Newcomb
Professor Pamela Abshire

© Copyright by
Nil Zeynep Gurel
2016

Acknowledgements

I want to thank Prof. Timothy Horiuchi for helping me through this work and keeping on advising me although nothing went as planned 1.5 years ago. For the experimental process, I deeply thank Dr. Joseph Conroy for being my ARL mentor, letting me use their laboratory and providing me with the key components used in the experiments and sharing his expertise. Witnessing Army Research Laboratory's collaborations with universities is something I am not familiar with in my country, I hope that we may also adopt these collaboration efforts and use the technology Turkey has in its army forces as a bridge to improve its own students, academicians and industry.

I had the opportunity to meet precious academicians throughout my two years at University of Maryland. Prof. Robert Newcomb and Prof. Pamela Abshire, thank you for accepting to be in my committee. Dr. Geoffrey Barrows, thank you for helpful discussions.

Badri, Lina, Imraan, Andrew, Mac, Ayan thank you for morale boosts and your friendship. My parents, Zerrin and Erdal Azmi Gurel, thank you for your unconditional support.

Prof. Yasemin Kahya, Faik Baskaya, Kadri Ozcaldiran and Selim Seker from Bogazici University, thank you for keeping in touch overseas. Prof. Gunhan Dundar, thank you for being an inspiration source to me, I really appreciate it.

Lastly, I thank Dr. Enrico Savazzi for the ultraviolet photos in the Appendix.

Table of Contents

Table of Figures

Chapter 1: Introduction

Motivation

The design of sensing mechanisms for small unmanned aircraft systems (sUAS) has many trade-offs due to limited budgets for power consumption, size, weight, and the need for both speed and accuracy in a wide range of operating conditions. Traditionally, inertial measurement units (gyroscopes and accelerometers) are used to obtain velocity and position data. There has been a rapid evolution of these sensor systems in recent years toward integrated accelerometer and gyroscope packages that include both digitization and signal conditioning (e.g. filtering). As the vehicle sizes have continued to decrease, faster sensing is needed due to the increased susceptibility of the aircraft to even tiny disturbances.

Looking to nature, several species of flying insects have been demonstrated to possess exceptional stability and acrobatic capabilities that match the types of missions that engineers are trying to accomplish. They provide examples of robust stability given similar limitations of sensing and processing. The insect body is a multimodal sensor network. Information from visual, proprioceptive, tactile and inertial receptors is collected to provide information about the state of the insect with respect to its environment [1]. Instead of the digital architecture used in traditional sUAS, insects have analog connections between their sensory systems and their flight motor neurons. Analog architecture makes them capable of closing feedback loops at high speeds, becoming very useful for fast stabilization for sudden disturbances. Bio-inspired sensing techniques based on these species present an attractive way for micro aerial vehicle sensor design.

Many flying insects employ two visual systems, the compound eyes and the ocelli (simple eyes). From the behavioral and electrophysiological experiments cited in the next chapters, the compound eyes and ocelli are thought to work together. Overall, compound eyes are sensitive to a wide-range of information, such as proximity to obstacles, relative velocity and rotation rate [5, 6, 20]. These tasks

increase the information processing time for the compound eyes, making them unable to provide fast responses for sudden disturbances. Insects have to balance themselves fast to survive. Ocelli, responsible for less number of tasks in compared to compound eyes, have less processing time [58,60], which makes them favorable to detect sudden disturbances. Inspired by the complementary nature of ocelli and compound eyes, this thesis attempts to characterize the frequency response of an ocellar sensor and optic flow, and ultimately proposes the fusion of two sensors for low-cost, wide-field, visual rotational motion sensing.

Contributions

The contributions of this thesis are listed as follows.

1. The comparative open-loop frequency characterization of optic flow and a luminance-dependent analog rotation rate sensor that is thought to mimic insect ocelli was conducted.
2. Sensitivity analysis was done to analyze the parameters that affect the optic flow and ocellar sensor performance in rotational motion.
3. The usability of ultraviolet intensity was analyzed to extend the usage of ocellar sensor to outdoors (Appendix A)

Outline of Thesis

Chapter 2 summarizes background information for compound eye, ocelli, previous engineering implementations of luminance-based sensors, chapter 3 demonstrates the frequency response characteristics of ocellar and optic flow sensing, chapter 4 discusses the complementary characteristics of optic flow and ocellar sensor and presents a complementary fusion from low-quality optic flow data and ocellar sensor data, chapter 5 presents conclusion & future work.
Additionally, appendix B discusses an ultraviolet vision approach and presents experimental data to understand the sky-ground discrimination in ultraviolet wavelengths.

Chapter 2: Background

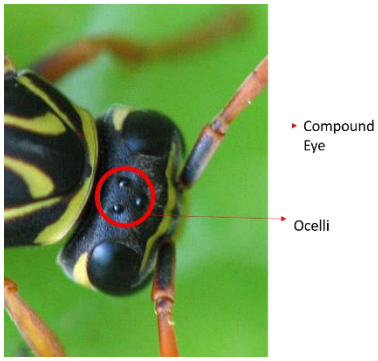

Figure 1: Insect Compound Eye and Ocelli (image from [2])

Structure and Function of Compound Eye

The compound eyes and ocelli are shown in Figure 1, head of a flying insect (Polistes). The structure of compound eyes (large, two on the sides) is seen in Figure 2. The compound eyes are composed of units called ommatidia. Each ommatidium unit functions as a separate visual receptor, consisting of a lens, cornea, a crystalline cone, light sensitive visual cells and pigment cells (Figure 3). There may be up to 30000 ommatidia in a single compound eye. The image perceived is a combination of inputs from ommatidia pointing at slightly different directions (as seen in Figure 2, ommatidia units make up a conic surface). A mosaic-like vision of the environment is rendered [5, 6].

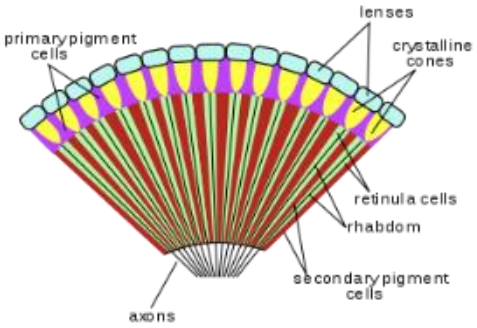

Figure 2: Structure of Compound Eye (image from [3])

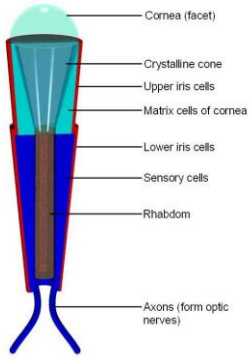

Figure 3: Structure of Ommatidium (image from [4])

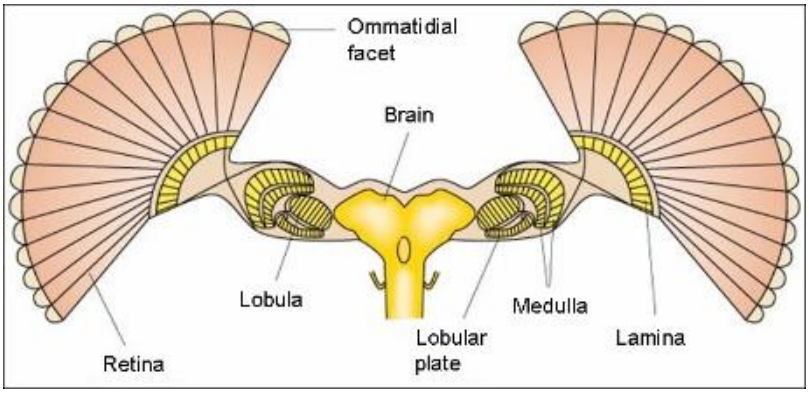

Figure 4: Ommatidia to Brain

Vision process starts at ommatidia. Ommatidia photoreceptors capture patterns of luminance from the visual environment. The captured signal is conditioned through lamina plate. The output of lamina is

thought to be the input to medulla [7,8]. The medulla outputs optic flow-like patterns to lobula, and lobula processes these outputs [9, 10, 11, 12, 13]. Figure 4 shows an illustration from ommatidia to lobula plate. The output signals of lamina neurons are segregated into different pathways, performing functions such as color discrimination, motion detection and intensity encoding. Neurons responding to motion are found in lobula. They are thought to receive inputs from hypothetical neural elements called Reichardt Detectors, or (elementary motion detectors (EMDs)) residing in medulla and calculating motion from the pixel-based information with a mechanism called Reichardt correlation [14]. This hypothetical mechanism is proposed to understand how a neuron, which is only receiving luminance input, is able to compute motion. The key components of this algorithm are two inputs (red, as photoreceptors), a time delay on one input (d), and multiplication on correlated signals.

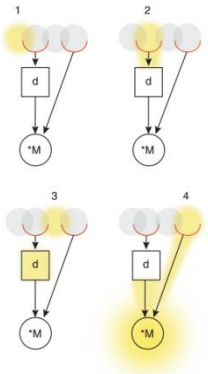

Figure 5: Schematic of Elementary Motion Detector (image from [15])

1. Photons from a visual scene move from left to right.
2. Photons activate the first receptor
3. The signal from the first receptor is delayed with d as the photons move to the second receptor
4. Photons activate the second photoreceptor. Both delayed signal (from first receptor) and un-delayed signal (from second receptor) converge simultaneously onto a multiplication stage, producing a signal related to direction of motion. Conversely, photons passing from right to

left will output zero for the opposite direction, since there is no delay component that will delivers simultaneous inputs to multiplication stage.

Structure and Function of Ocelli

Ocelli differ from the compound eye in having only a single lens covering an array of photoreceptors, seen in Figure 6. Ocelli are found in the frontal surface of the head of many insects. Ocelli tend to be larger in flying insects (bees, dragonflies, locusts). They are typically found as a triplet. Two lateral ocelli are found in the left and right of the head, while a median ocellus is directed frontally.

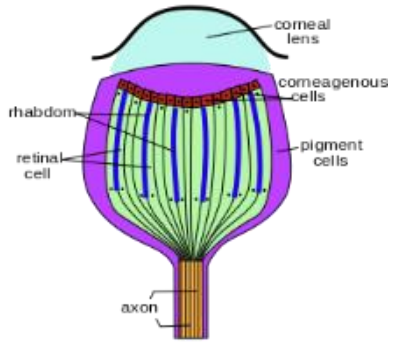

Figure 6: Ocellus Cross Section (image from [16])

Various studies have been conducted to reveal the function of ocelli, for different insects. Although it is called an 'eye', ocellus is claimed to be under-focusing the image, hence showing hardly any image details for a locust. In contrast to the 'under-focusing' information for locust, [17] suggests that dragonfly ocellus, which is believed to have a highly evolved ocellus, is able to detect some image details.

It is also suggested that the temporal and spatial filtering characteristics of locust ocelli neurons are well suited to detect instability in flight [18, 19]. The stabilization in flight studies were summarized in [20], most of which are conducted by releasing dragonflies with ablated ocelli. Dragonflies show unstable flight attitudes without ocelli. [21] evaluates the flight behavior of bees with and without occluded ocelli, stating that normal bees (without occlusion) show quicker flight behaviors.

Another characteristics of ocellus is reported as the higher photic sensitivity, compared to compound eye (18] for locusts and [22] for bees). This information is useful if we think of the ocelli as integrators of the overall intensity or a blurred visual field. If the photic sensitivity is high, small changes in light intensity will be sensed. Taking into account that the images sensed by the ocelli are highly blurred, ocelli should be concerned with the overall image intensity. [23, 24] for dragonflies and [25] for locusts claim that ocelli are rotation detectors important for gaze stabilization. [26] also shows gaze stabilization cues by the ocelli. The beginning and end of daily activities of insects depend on light intensity. [22] for bees, [27] for crickets, and [28, 29,30] for moths claim that the ocelli perceive low light intensity to control daily activities.

Compared to ocelli, compound eyes offer a panoramic field of view and high temporal resolution, with optic flow computation abilities [31, 32, 33]. These features are beneficial for tasks like visually guided navigation, e.g. obstacle avoidance, landing strategy, saccade response, hovering strategy clutter response, collision response and fixation strategy, each of which are described in [34] with specific test setups for bees and drosophilae.

Prior Work Inspired by Insect Ocelli

Because of the prominent computation advantages, simplicity and applicability to small-scale world, ocelli-inspired vision sensors have been developed by many groups. These implementations mainly focus on closed-loop attitude control, outputting pitch and roll angle. [35] presents a simulation model of an autonomous agent flying through a virtual environment with a daylight sky model. It uses over two hundred receptors to detect local intensities. These receptors are distributed evenly between adjacent directions on agent body coordinate system. The average intensity difference between two directions are computed to estimate the roll angle. Subsequently, a simulation of an eye model with a special receptor distribution was presented in a virtual environment in [36]. The ocelli-like ‘wide-field measurement units’ that use a locally weighted intensity as receptor response are subtracted in adjacent directions. Using elementary motion detector (described in Compound Eye section) and ocelli outputs,

optimal receptive fields for attitude estimation, yaw rotations and nearness are derived. [37] implements ocelli, haltere (an organ responsible for balance in flying insects), optic flow and magnetic flow sensors for a micromechanical flying insect. These sensors were used to estimate body attitude relative to a fixed frame, body rotational velocities, obstacle avoidance and heading adjustment, respectively. The ocelli consist of four photodiodes, arranged in a pyramidal configuration. The two output signals are obtained by subtracting the opposite photodiode outputs. [38] uses this implementation and proposes a stabilizing attitude control law for a sinusoidal intensity function. [39] demonstrates an embedded implementation of ocelli-like sensor. It uses the difference between ultraviolet and green photodiode signals to obtain attitude estimation, stating that this reduces the biasing effect of clouds and the sun. [40] uses a camera to track a reference heading point and performs gaze stabilization by using the difference between reference and instantaneous heading signal. [41] uses camera images that are classified by the intensity information in YUV (luminance, blue, red) channel into sky and ground regions to estimate roll and pitch angles. [42] uses four ultraviolet/green photodiode pairs to detect attitude angle and demonstrates roll attitude tracking on an aircraft. [43] proposes an ocelli-based sensor, which is also used in this work, to output roll and pitch rate, rather than angle. This sensor is used for the frequency characterization in chapter 3.

Chapter 3: Frequency Domain Characterization of An Ocellar Sensor and Optic Flow

Introduction

Gremillion et al. [43] present experimental data that utilizes the complementary response of an analog ocellar sensor and a commercial optic flow sensor. Inspired by this complementary response information and cues from insect ocelli and compound eye complementary task mechanism, we designed a test platform that generates rotational motion to characterize the frequency-domain response of both optic flow and an ocellar sensor, and gathers information from different sources such as motor controller, microcontroller and gyroscope. The optic flow is computed using the images collected by a camera and fisheye lens. A MEMS gyroscope and a Vicon^{TM} motion detection system are used as ground truth. This chapter discusses the ocelli and optic flow frequency response characteristics and the performance parameters for the ocelli and optic flow computation.

Ocellar Sensor

The ocellar sensor (based on work by Gremillion et al., [43]) gives roll and pitch rate estimates using the luminance change sensed by right-left or front-back photodiode pairs. The luminance signals from left (aft) and right (front) photodiodes are band-pass. The high-pass filter portion serves as the differentiator element, to estimate rate information introduced by luminance change. The high-frequency cutoff was added to reject the flickering noise for indoors usage. The filtered signals from the photodiodes are antagonistically subtracted from each other (left-right or front-back), to obtain roll and pitch rate estimates. The overall circuit schematics are shown in Figure 7 and the circuit components are listed in Table 1.

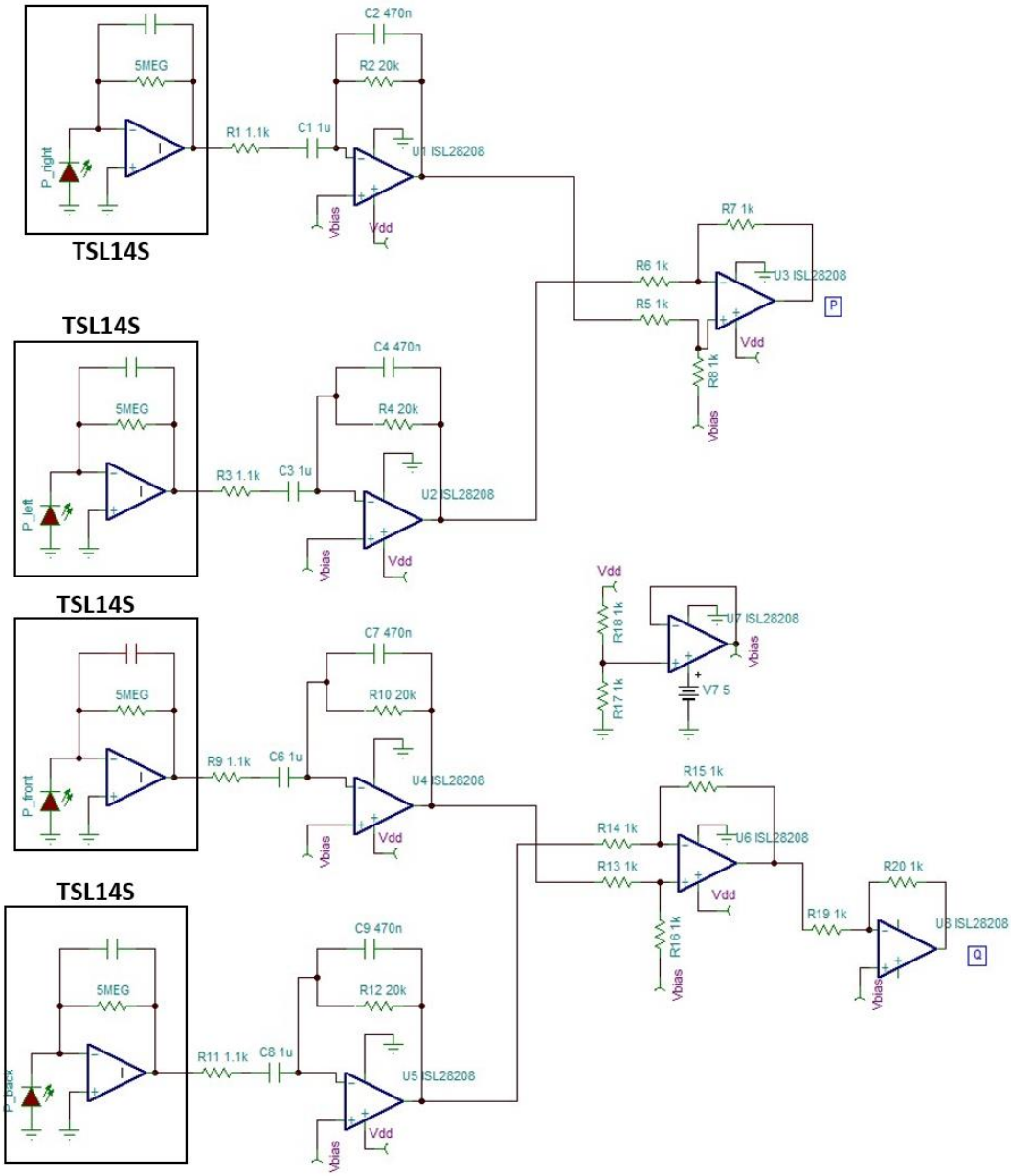

Figure 7: Circuit schematics of the three stage ocellar sensor. TSL14S photodiode outputs are band-pass filtered and antagonistically subtracted. Pitch rate (front-back) is inverted for sign change.

Table 1: Circuit Components

Component	Value/Part Number
R1,3,9,11	1.1kΩ
R5,6,7,8,13,14,15,16,17,18,19,20	1 kΩ
R2,4,10,12	20 kΩ
C1,3,6,8	1μF
C2,4,7,9	470nF
Operational Amplifier	ISL28208
Photodiode	TSL14S
Vdd	5V

The circuit consists of three stages:

1. Light-to-Voltage Conversion

Light-to-voltage conversion by a TSL14S optical sensor [91] that combines a photodiode and a trans-impedance amplifier. The sensor has a wide-band spectral response characteristics between 320-1050 nm. Its peak output is at 640nm. The output voltage from this element is the electrical equivalent of luminance seen by the photodiode.

2. Band-Pass Filtering

This stage consists of an active band-pass filter with a designed high-pass cutoff at 17 Hz and low-pass cutoff at 145 Hz (See Figure 8).

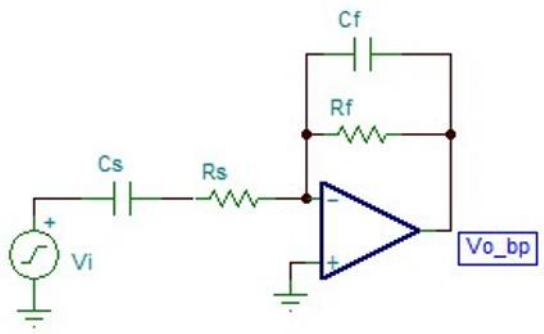

Figure 8: Band-pass filter, with high-pass cutoff at 17 Hz and low-pass cutoff at 145 Hz.

The input-output relationship of a high-pass filter is modeled as:

$$V_o(t) = -R_f C_s \frac{d}{dt}\left(V_i(t)\right) \qquad (1)$$

The input voltage is the luminance value from TSL14S package. The output voltage approximates the luminance time rate of change. The function of the low-pass filter is to attenuate high-frequency noise. The final band-pass filter transfer function is in equation (2).

$$\frac{V_o(s)}{V_i(s)} = \frac{sC_sR_F}{s^2C_FR_FC_SR_S + s(C_FR_F + C_SR_S) + 1} \qquad (2)$$

The characteristic quantities of this second order transfer function are the low-pass cutoff frequency ω_L, high-pass cutoff frequency ω_H and maximum input-output gain A_{max}, specified in Table 2.

Table 2: Band-Pass Filter Characteristics

$\omega_L = \frac{1}{R_FC_F}$	106 rad/s (16.9 Hz)
$\omega_H = \frac{1}{R_SC_S}$	909 rad/s (145 Hz)

$A_{max} = \frac{-R_F}{R_S}$	-18.2

3. Linear combination stage:

This stage includes a difference amplifier to subtract right-left filter outputs and front-back filter outputs. The difference amplifier output from the right-left inputs estimates the roll rate. The difference amplifier output from the front-back inputs is inverted (for sign change) by an inverting amplifier. Inverting amplifier output estimates the pitch rate (See the blocks in Figure 9).

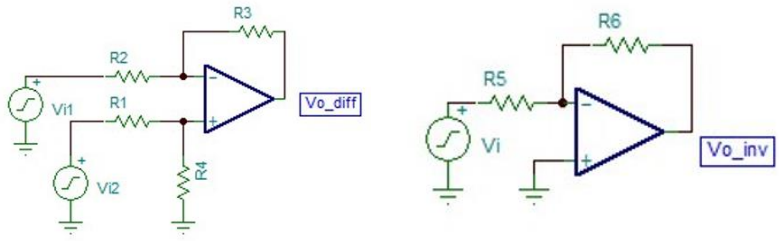

Figure 9: Subtractor and inverter: Subtractor is used for antagonistic subtraction of filtered signals. Inverter is used for sign change for pitch rate. For equal resistors in both blocks, direct subtraction and direct inversion is satisfied.

For $R_{1,2,3,4,5,6}$ =1kΩ, the outputs V_{o_diff} and V_{o_inv} are modeled as:

$$V_{o\_diff} = V_{i2} - V_{i1} \qquad (3)$$

$$V_{o\_inv} = -V_i \qquad (4)$$

The band-pass filter was simulated (Figure 10) using the macro model of the ISL28208 operational amplifier in the Tina TI SPICE-based simulation program. The simulated circuit and AC transfer characteristics for frequencies between 1 mHz and 1 Megahertz is seen in Figure 11. According to the simulation (due to the zero in the denominator of the transfer function) the amplitude is increases by 20dB/decade until it hits the first pole. The high-pass -3dB frequency is seen as 13 Hz. The maximum amplitude is 5.58dB around 55 Hz. The low-pass -3dB frequency is seen as 175 Hz.

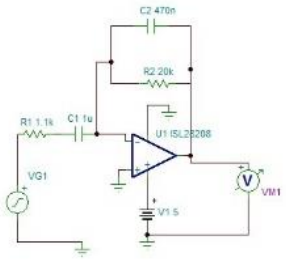

Figure 10: Simulated circuit in TI TINA Simulation Software.

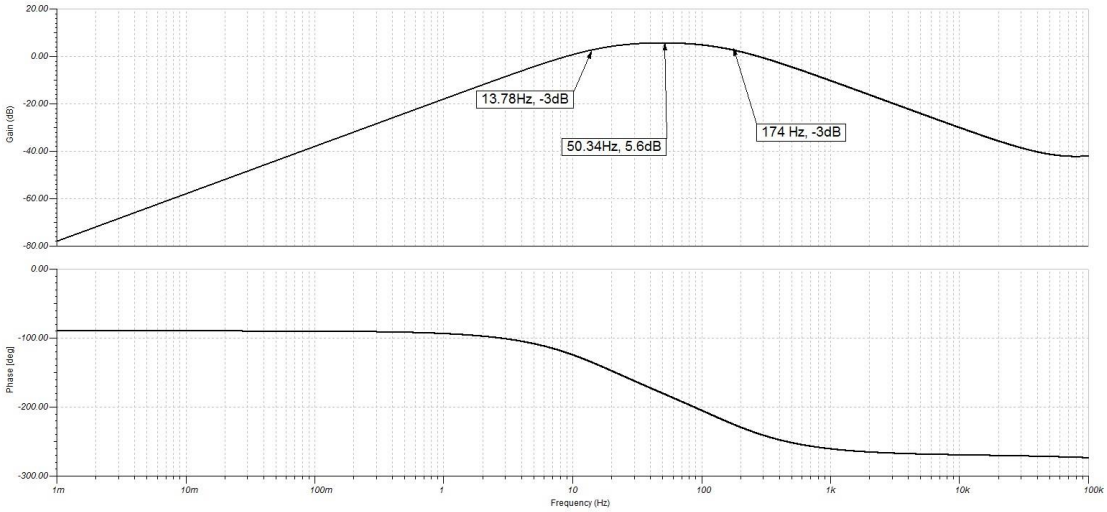

Figure 11: Band-pass filter simulation results: 13.78 Hz high-pass cutoff and 174 Hz low-pass cutoff is observed. Phase starts at -90^0 at 1 mHz and reaches to -270^0 at 100 kHz.

Mathematical Model for the Ocellar Sensor

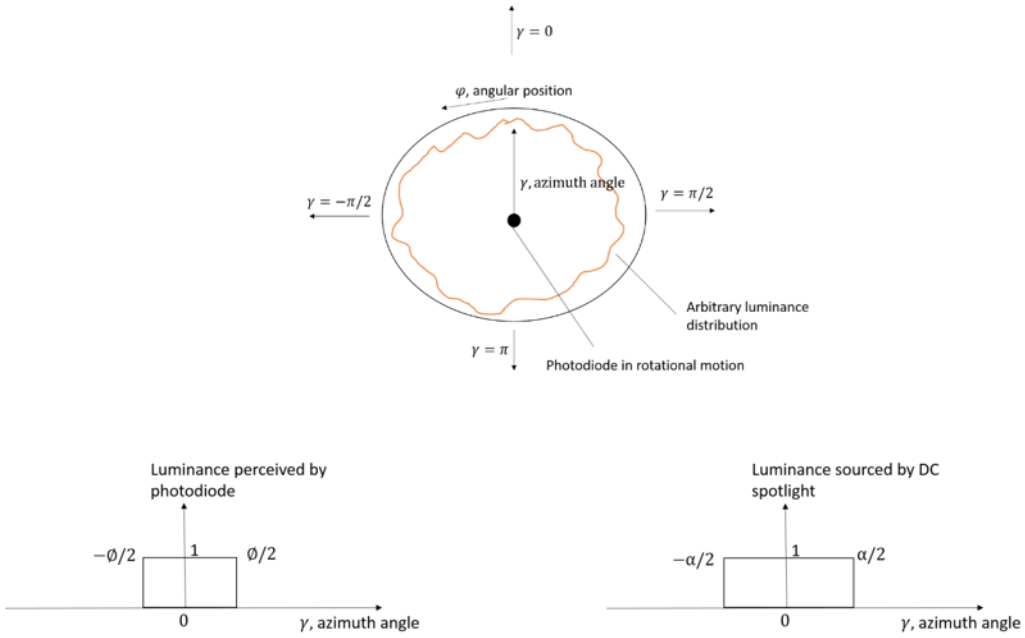

Figure 12: Mathematical Model and Assumptions: Photodiode in rotational motion sees the arbitrary luminance pattern as its azimuthal angle varies.

With reference to Figure 12, the variables used to explain the ocellar sensor are as follows:

γ: $Azimuth\ angle$ of the photodiode.

φ: $Angular\ position$

$\emptyset$: $Photodiode\ field\ of\ view$

$\vartheta = \frac{d\gamma}{dt} = \dot{\gamma}$: $Angular\ speed$

$L(\gamma)$: $Luminance, assume\ periodic$

α: $Light\ source\ field\ of\ luminance$

The test setup has a DC spotlight source, which acts as 'the sun'. For simplicity, luminance is modeled as a rectangular function with fixed edges from - $\alpha/2$ to $\alpha/2$. Photodiode field of view is also modeled as a rectangular function with edges at field of view edges, $-\emptyset/2$ to $\emptyset/2$

$h(\emptyset, \gamma)$: $Photodiode\ field\ of\ view\ function, modeled\ as\ a\ rectangular\ filter\ with\ edges\ at$

$-\emptyset/2\ and\ \emptyset/2$

ρ: *Photodiode output (or signal input to bandpass filter)*

$*$: *convolution operation*

The photodiode integrates the luminance in its field of view, as $h(\emptyset, \gamma)$

$$\rho = \int_{FOV} L(\gamma) d\gamma = L(\gamma) * h(\emptyset, \gamma) = L_h(\gamma) \qquad (5)$$

Let $L_h(\gamma)$ be a photodiode output taken at the azimuth angle γ. While the circuit is in rotational motion with angular speed ϑ, this photodiode output becomes $L_h(\gamma - \vartheta t)$ at time t. Thus, the photodiode output encodes both spatial (γ) and temporal (ϑt) information.

$$L_h(\gamma) \rightarrow L_h(\gamma - \vartheta t) \qquad (6)$$

Since the photodiode output is in two domains, the Fourier transform with respect to both spatial and temporal variables should be taken in order to express it in Fourier domain.

$L_h(\gamma, t)$: *denotes the function in spatial and temporal domain*

$\widehat{L_h}(f_\gamma, f_t)$: *denotes the Fourier transform of* $L_h(\gamma, t)$

$$L_h(\gamma - \vartheta t) \overset{FT_{\gamma,t}}{\Longleftrightarrow} \widehat{L_h}(f_\gamma, f_t) \qquad (7)$$

Properties used:

Shifting property in time/space and Fourier domain:

$$x(\gamma - \beta) \overset{FT_\gamma}{\Longleftrightarrow} \hat{X}(f_\gamma) e^{-j2\pi f_\gamma \beta} \qquad (8)$$

Convolution:

$$x(\gamma) * y(\gamma) \overset{FT_\gamma}{\Longleftrightarrow} \hat{X}(f_\gamma)\hat{Y}(f_\gamma) \qquad (9)$$

1) Taking the Fourier transform with respect to spatial variable γ:

$$L_h(\gamma - \vartheta t) \overset{FT_\gamma}{\Longleftrightarrow} \widehat{L_h}(f_\gamma) e^{-j2\pi(\vartheta f_\gamma)t} \qquad (10)$$

2) Then, taking the Fourier transform with respect to temporal variable t gives the frequency domain of a rotational motion:

$$\widehat{L_h}(f_\gamma, f_t) = \widehat{L_h}(f_\gamma)\delta(f_t + \vartheta f_\gamma) \qquad (11)$$

Thus,

$$L_h(\gamma - \vartheta t) \overset{FT_{\gamma,t}}{\Longleftrightarrow} \widehat{L_h}(f_\gamma)\delta(f_t + \vartheta f_\gamma) \qquad (12)$$

This means that all the energy of the rotating photodiode output is contained in a plane of the spatio-temporal frequencies domain [44,45]. The equation of this plane is:

$$f_t + \vartheta f_\gamma = 0 \qquad (13)$$

Figure 13 shows a representation of a rectangular luminance function $L_h(\gamma - \vartheta t) \sim rect(x,t)$ with space and time axis ($\gamma \rightarrow$x). A rectangular pulse in space rect(x) has sinc form in frequency domain:

$$rect(x) \overset{FT_x}{\Leftrightarrow} \frac{\sin(\pi f_x)}{\pi f_x} \qquad (14)$$

The corresponding frequency spectrum of this moving pulse is given as the black curve in the figure 13. It appears as a cut of spatial spectrum $\frac{\sin(\pi f_x)}{\pi f_x}$ by a wall of Dirac situated in the direction of $f_t + \vartheta f_x = 0$ (for this case, $f_t + \vartheta f_\gamma = 0$)

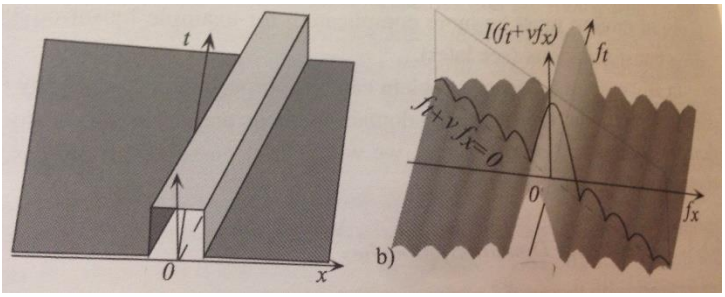

Figure 13: Frequency spectrum of a rectangular in spatio-temporal domain: (Left) Example of a moving 1-D spatial rectangular shape, moving in the spatio-temporal domain. (Right) Its spatio-temporal frequency spectrum (black curve) as a 'cut' of the purely spatial Fourier transform of the rectangle by a 'Wall of Dirac'. Image taken from [46]]

Overall,

$$\widehat{L_h}(f_\gamma, f_t) = \widehat{L_h}(f_\gamma)\delta(f_t + \vartheta f_\gamma) \qquad (15)$$

(15) represents the photodiode output given as input to the band pass filter in the circuit. Band-pass filtering is a temporal process, thus the band pass function has only temporal variable. Let the band pass filter transfer function in time and Fourier domain be defined as:

$$BPF(t) \overset{FT_t}{\Leftrightarrow} \widehat{BPF}(f_t) \ or \ \widehat{BPF}(s) \qquad (16)$$

From the ocellar sensor section $\widehat{BPF}(s)$ is defined as

$$\widehat{BPF}(s) = \frac{V_o(s)}{V_i(s)} = \frac{sC_sR_F}{s^2C_FR_FC_SR_S + s(C_FR_F + C_SR_S) + 1} \qquad (17)$$

The output of the band pass filter can be written as:

$$L_{h,BPF}(\gamma, t) = L_h(\gamma - \vartheta t) * BPF(t) \qquad (18)$$

The Fourier transform of the output becomes:

$$L_{h,BPF}(\gamma, t) \overset{FT_{\gamma,t}}{\Longleftrightarrow} \widehat{L_{h,BPF}}(f_\gamma, f_t) \qquad (19)$$

$$L_h(\gamma - \vartheta t) * BPF(t) \overset{FT_{\gamma,t}}{\Longleftrightarrow} \widehat{L_h}(f_\gamma)\delta(f_t + \vartheta f_\gamma)\widehat{BPF}(f_t) \qquad (20)$$

This output represents the luminance output filtered by one photodiode. Assume another photodiode is has a different azimuth angle, $\gamma - \beta$, offset by β from the first photodiode. The luminance perceived by it will be:

$$L_{h,\beta}(\gamma - \beta - \vartheta t) \overset{FT_{\gamma,t}}{\Longleftrightarrow} \widehat{L_{h,\beta}}(f_\gamma, f_t, \beta) \qquad (21)$$

$$L_{h,\beta,BPF}(\gamma, t, \beta) \overset{FT_{\gamma,t}}{\Longleftrightarrow} \widehat{L_{h,\beta,BPF}}(f_\gamma, f_t, \beta) \qquad (22)$$

$$\widehat{L_{h,\beta}}(f_\gamma, f_t, \beta) = \widehat{L_{h,\beta}}(f_\gamma)\delta(f_t + \vartheta f_\gamma)e^{-j2\pi f_\gamma \beta} \qquad (23)$$

After band pass filtering, the Fourier transform of the second output becomes:

$$\widehat{L_{h,\beta,BPF}}(f_\gamma, f_t, \beta) = \widehat{L_{h,\beta}}(f_\gamma)\delta(f_t + \vartheta f_\gamma)e^{-j2\pi f_\gamma \beta}\widehat{BPF}(f_t) \qquad (24)$$

The difference amplifier implements direct subtraction between two band pass filter outputs as the roll rate estimation. Let the roll rate be denoted as p(γ,t)

$$\mathrm{p}(\gamma, \mathrm{t}) = L_{h,BPF}(\gamma, t) - L_{h,\beta,BPF}(\gamma, t) \qquad (25)$$

$$\mathrm{p}(\gamma, \mathrm{t}) \overset{FT_{\gamma,t}}{\Longleftrightarrow} \widehat{\mathrm{P}}(f_\gamma, f_\mathrm{t}) \qquad (26)$$

$$\begin{aligned}\widehat{\mathrm{P}}(f_\gamma, f_\mathrm{t}) &= \widehat{L_{h,BPF}}(f_\gamma, f_t) - \widehat{L_{h,\beta,BPF}}(f_\gamma, f_t, \beta) \\ &= \widehat{L_h}(f_\gamma)\delta(f_t + \vartheta f_\gamma)\widehat{BPF}(f_t) - \widehat{L_{h,\beta}}(f_\gamma)\delta(f_t + \vartheta f_\gamma)e^{-j2\pi f_\gamma \beta}\widehat{BPF}(f_t) \\ &= \widehat{BPF}(f_t)\delta(f_t + \vartheta f_\gamma)[\widehat{L_h}(f_\gamma) - \widehat{L_{h,\beta}}(f_\gamma)e^{-j2\pi f_\gamma \beta}] \qquad (27)\end{aligned}$$

Thus, the circuit output depends on:

- Photodiode field of view

- Band pass filter characteristics
- Luminance function $L(\gamma)$
- Photodiode angular separation β

The photodiode field-of-view and band pass filter characteristics are inherent in the circuit under test and these variables are fixed. We have control of the luminance function $L(\gamma)$ and photodiode angular separation β. The luminance function is also dependent on the light intensity (or, the input power given to light source).

Optic Flow Computation

Optic flow is an approximation of apparent motion of brightness patterns observed when an observer (i.e. camera) is moving relative to the objects it images. Optic flow methods try to calculate where a pixel in image A goes to in a consecutive image B. In two-dimensions (2-D), optic flow specifies how much a pixel of an image moves between adjacent series [47]. The basis of optic flow is the brightness constancy equation, which eventually forms the 2D motion constraint.

Assume that I(x,y,t) is the intensity of pixel positioned at location (x,y) in a frame taken at time t. In the frame taken at time (t+Δt), this pixel moves to the location (x+Δx, y+Δy) (See Figure 14).

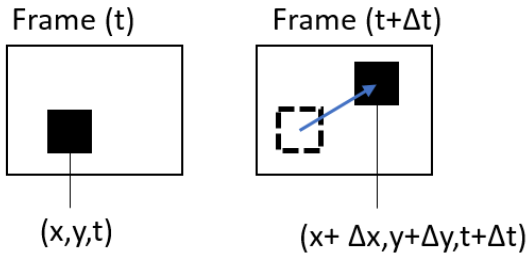

Figure 14: Optic flow vector for a pixel between two consecutive frames

Assuming the brightness of the pixel does not change over time;

$$I(x, y, t) = I(x + \Delta x, y + \Delta y, t + \Delta t) \qquad (28)$$

Performing 1st order Taylor Series expansion about I (x, y, t):

$$I(x+\Delta x, y+\Delta y, t+\Delta t) = I(x,y,t) + \frac{\partial I}{\partial x}\Delta x + \frac{\partial I}{\partial y}\Delta y + \frac{\partial I}{\partial t}\Delta t + higher\ order\ terms \quad (29)$$

Assuming very small motion and ignoring the higher order terms,

$$\frac{\partial I}{\partial x}\Delta x + \frac{\partial I}{\partial y}\Delta y + \frac{\partial I}{\partial t}\Delta t = 0 \quad (30)$$

Dividing everything by Δt:

$$\frac{\partial I}{\partial x}\frac{\Delta x}{\Delta t} + \frac{\partial I}{\partial y}\frac{\Delta y}{\Delta t} + \frac{\partial I}{\partial t}\frac{\Delta t}{\Delta t} = 0 \quad (31)$$

Denoting:

$$\frac{\partial I}{\partial x} = I_x,\ \frac{\partial I}{\partial y} = I_y,\ \frac{\partial I}{\partial t} = I_t \quad (32)$$

$$\frac{\Delta x}{\Delta t} = \vartheta_x \qquad \frac{\Delta y}{\Delta t} = \vartheta_y$$

$$I_x V_x + I_y V_y + I_t = 0 \quad (33)$$

Here, V_x and V_y are the x and y components of optic flow (for the motion described in Figure 14). The equation can be written more compactly as:

$$\left(I_x, I_y\right) \cdot \left(\vartheta_x, \vartheta_y\right) = I_t \quad (34)$$

$$\nabla I \cdot \vartheta = -I_t \quad (35)$$

where $\nabla I = \left(I_x, I_y\right)$ is the spatial intensity gradient and $\vartheta = \left(\vartheta_x, \vartheta_y\right)$ is the velocity of the pixel (x,y) at time t. Equation 35 is called the 2D motion constraint equation. This equation has two unknowns $(\vartheta_x, \vartheta_y)$, which relates to the aperture problem. If the motion detector's aperture is much smaller than the contour it observes, it can be only sensitive to the component of the contour's motion that is perpendicular to the edge of the contour. It is blind to any motion parallel to the contour. This is because the movement in this direction will not change the appearance of anything within the aperture. To find optic flow vectors, additional equations are needed. Many optic flow computation methods focus on additional constraints that attempt to recover the optic flow vectors. [48] assumes that the displacement of the image contents between two frames is constant within a neighborhood of a point

under consideration. [49] assumes smoothness in the flow over the whole image and prefers solutions which show more smoothness.

For the Lucas-Kanade motion algorithm [48], the 2D motion constraint equation is assumed to hold for all pixels within a window centered at p. This means that the motion constraint equation holds for all the pixels in a window with the same unknowns $\vartheta = (\vartheta_x, \vartheta_y)$. This set of equations bring an over-determined system that has more equations than unknowns:

$$I_x(q_1)\,\vartheta_x + I_y(q_1)\,\vartheta_y = -I_t(q_1)$$

$$I_x(q_2)\,\vartheta_x + I_y(q_2)\,\vartheta_y = -I_t(q_2)$$

$$\dots\dots \qquad \dots\dots \qquad \dots\dots$$

$$\dots\dots \qquad \dots\dots \qquad \dots\dots$$

$$\dots\dots \qquad \dots\dots \qquad \dots\dots$$

$$I_x(q_n)\,\vartheta_x + I_y(q_n)\,\vartheta_y = -I_t(q_n)$$

Where $q_1, q_2, \dots..q_n$ are the pixels inside the window. In matrix form:

$A\vartheta = b$ where,

$$A = \begin{bmatrix} I_x(q_1) & I_y(q_1) \\ I_x(q_2) & I_y(q_2) \\ \vdots & \vdots \\ I_x(q_n) & I_y(q_n) \end{bmatrix}$$

$$\vartheta = \begin{bmatrix} \vartheta_x \\ \vartheta_y \end{bmatrix}$$

$$b = \begin{bmatrix} -I_t(q_1) \\ -I_t(q_2) \\ \vdots \\ -I_t(q_n) \end{bmatrix}$$

Least squares principle can be applied to solve this over-determined system:

$$A^T A\vartheta = A^T b \qquad (36)$$

$$\vartheta = (A^T A)^{-1} A^T b \qquad (37)$$

$$\begin{bmatrix}\vartheta_x \\ \vartheta_y\end{bmatrix} = \begin{bmatrix} \sum_i I_x\,(q_i)^2 & \sum_i I_x\,(q_i) I_y\,(q_i) \\ \sum_i I_y\,(q_i) I_x(q_i) & \sum_i I_y\,(q_i)^2 \end{bmatrix}^{-1} \begin{bmatrix} -I_x\,(q_i) I_t\,(q_i) \\ -I_y\,(q_i) I_t\,(q_i) \end{bmatrix} \quad (38)$$

Optic flow vectors ϑ_x and ϑ_y are searched in a tracking window and the best match is found using the least squares method. This system is solvable if $A^T A$ is invertible. The eigenvalues of $A^T A$ ($\lambda_1, \lambda_2\ where\ \lambda_1 > \lambda_2$) should not be too small, and $A^T A$ should be well-conditioned ($\frac{\lambda_1}{\lambda_2}$ should not be too large), so $\lambda_1 > \lambda_2$ should be somewhat similar to each other in magnitude. In other words, very small eigenvalues are interpreted as 'flat surfaces', eigenvalues $\lambda_1 \gg \lambda_2$ or $\lambda_1 \ll \lambda_2$ are interpreted as 'edges'. Optimum eigenvalues should be large enough and have similar amplitude [50].

One drawback of the Lucas-Kanade algorithm is that it theoretically fails for large motions. If the motion is too large, higher order terms may dominate the equation (29) (The 1st order Taylor Series Expansion). Reducing the image resolution may solve this issue. A pyramidal approach is available to convert large motions to small motions [51]

Different optic flow computation methods can be described as either 'dense' and 'sparse'. From a performance point of view, dense computation methods (e.g. [49] and [52]) that process all of the pixels in the image are slow for real-time applications. Instead, sparse techniques (i.e. [48]) only process the pixels of interest. For real-time applications that use optic flow computation to feed the current state of an object back to a control loop, sparse techniques may be preferred over dense techniques due to faster computational performance (and thus higher sampling rate). In practice, we achieved 60 frames-per-second (fps) using the Lucas-Kanade algorithm but only 13 fps for the Farneback algorithm (376*240 pixels 8-bit monochromatic image sequence). For this work, the Lucas-Kanade algorithm is used with pre-defined feature points distributed over the imagery. The feature points are the center pixel points to run the Lucas Kanade algorithm for determining an optic flow vector. As the number of feature points increase, the number of optic flow vectors increase. The x-component of optic flow vectors are summed to obtain a single optic flow value.

Experimental Setup

In general, from Figure 15, the optic flow experienced by an imager is [34]:

$$Optic\ Flow = -\omega + (V/D)\ cos\theta \qquad (39)$$

where ω is the angular and V is the translational velocity of the vehicle, D is the distance to an object, θ is the angle between direction of travel and direction of object. If the translational component (V) is zero, optic flow is proportional to the angular velocity.

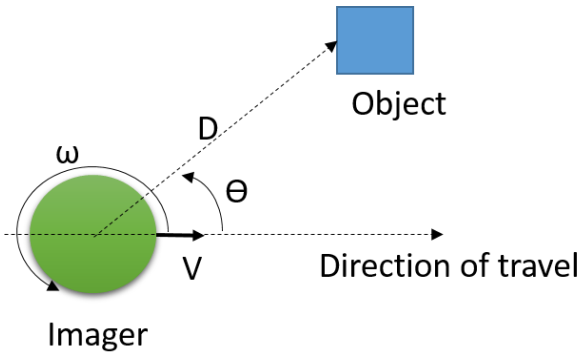

Figure 15: Optic flow during rotational and translational motion: Without translational component (V), optic flow is an estimate of only angular velocity (ω).

A mechanism was constructed to characterize optic flow and ocellar sensor over 0.1-10Hz rotational mechanical input. Figure 16 shows the illustration of the test setup; Figure 17 shows the scene the camera sees; Table 3 shows the system components and Figures 18 and 19 show the general and close-up view of the components. The block diagram of the system is shown in Figure 20.

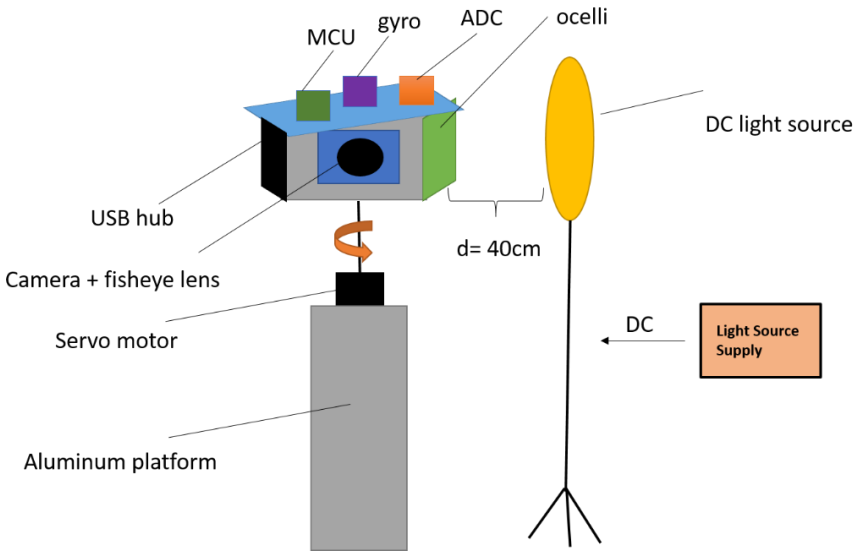

Figure 16: Illustration of Test Setup: Light source has its own DC supply to avoid issues of flickering. Information from camera, MCU, gyro, ADC are transferred to the host computer via a USB hub.

Figure 17: Camera scene (376*240 pixel image). DC light source is not in the field of view of the camera. Camera is moving along the x-direction

Table 3: Experiment Components

Equipment	Model/ Manufacturer
Light Source	LED1 OOWA-56 LED Video Light

Light Source Supply	GW-Instek-PSW-8027 Programmable Switching DC Power Supply
Motor	Animatics Smartmotor SM2340D
Motor Supply	PS42V6AG-110, 251 W, Moog, Animatics
Signal Generator	Tektronix AFG3252
Camera	UEYE UI-1221LE-M-GL USB 2.0,752x480, CMOS mono, 87.2 fps, 8-bit
Lens	Sunex DSL227 Miniature Superfisheye Lens, 180^{o} Field of view (FOV)
Microcontroller	Arduino UNO
ADC	MCP3008 8-channel 10-bit ADC with SPI
USB Hub	Hosa Technology
Gyroscope	Pololu MinIMU-9 v3 chip contains L3GD20H 3-axis gyro

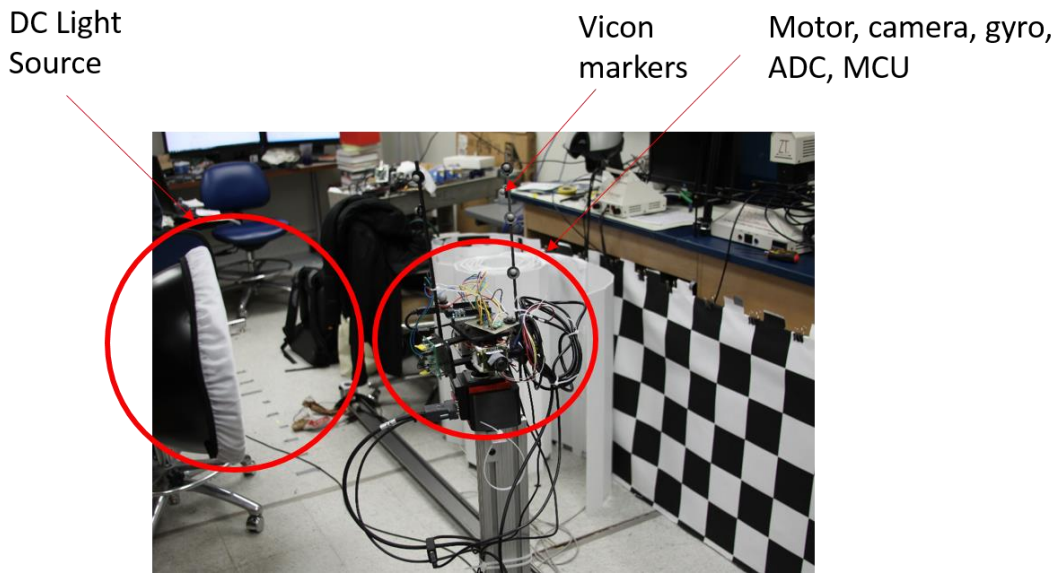

Figure 18: Overall test setup: Ocellar sensor is positioned in front of light source. Motor is giving rotational motion to the setup along its shaft axis. The motor shaft is in vertical orientation, moving the components on it.

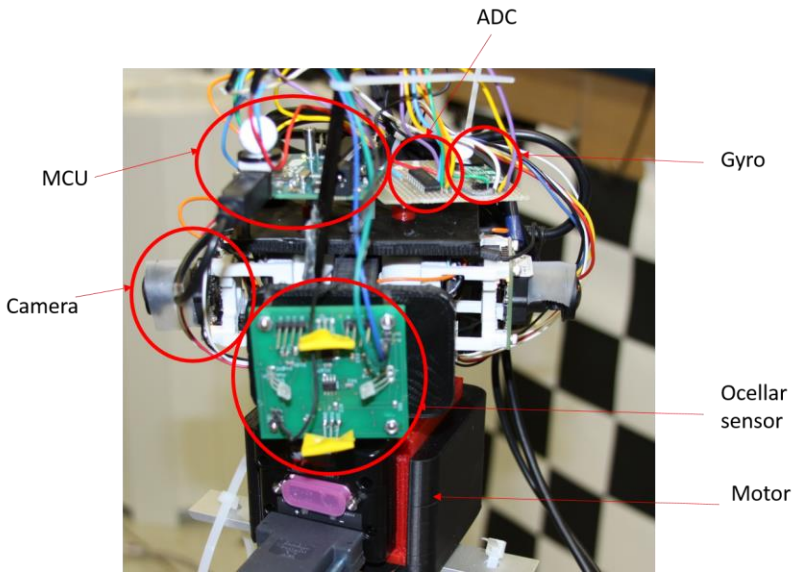

Figure 19: Test setup components: Camera sees the scene shown in Figure 17. Camera on the right is not used due to performance issues.

All data is stored in a laptop running Ubuntu 14.04 environment. Robot Operating System (ROS) environment us used to implement robot software. ROS is an open-source network for writing robot software, including a collection of tools, libraries and conventions. It allows for compact storage and data publishing from multiple peripherals. For this system, each component is represented by a different ROS 'node', that allows for the compilation of multiple C++ files and stores data in a 'bag' file. Once the data is collected, the bag file is 'unbagged' and parsed to extract the data.

To record the ocellar sensor analog voltage outputs, an analog-to-digital converter (ADC) board is used. For ground truth, an 16-bit gyroscope is also used. The ADC board (MCP3008) communicates with the Arduino UNO microcontroller via serial peripheral interface (SPI). Gyroscope communication is through inter-integrated circuit technology (I^2C). The microcontroller is programmed in C language. It reads ADC and gyroscope outputs, parses the values into most significant (MSB) and least significant (LSB) bytes. Each sample consists of one MSB and one LSB (i.e., a two byte word). A message is created (See Figure 21) with two header bytes to be sent to the laptop via serial

communication at 115200 bps. A 15 microsecond delay is added between each byte sent to allow the receiver buffer to be cleared to avoid overwriting.

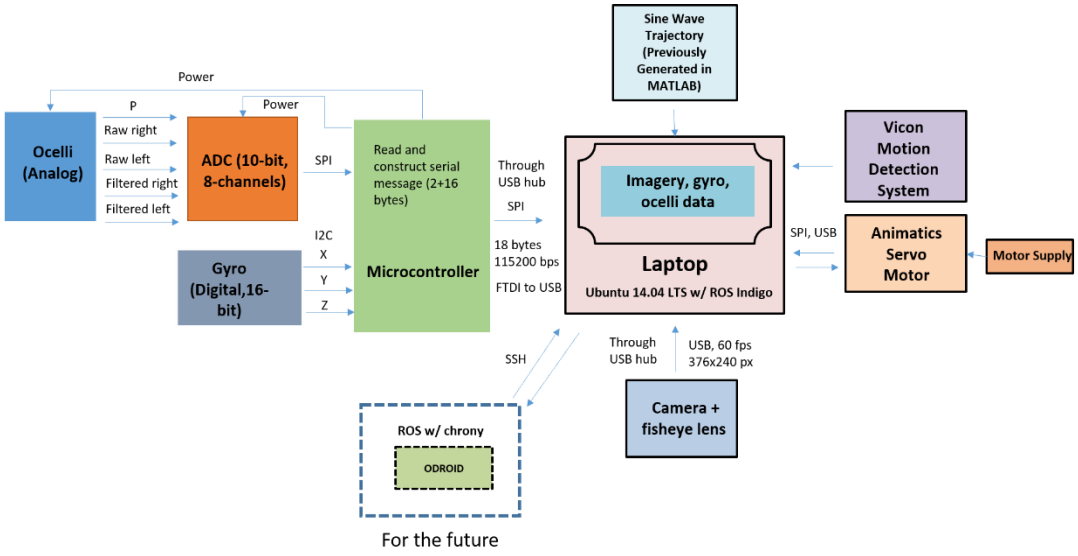

Figure 20: System block diagram: All the data collected is stored in laptop.

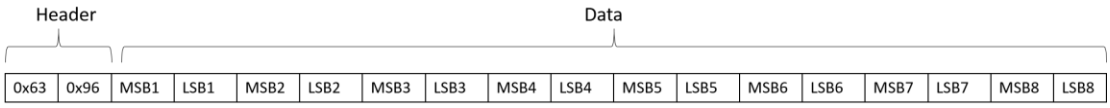

Figure 21: Serial message structure from ocelli to microcontroller: It includes two header, ocelli data and gyro data bytes.

The servo motor can be operated in either position or velocity mode. Velocity mode does not offer control in position. Motor is controlled by sending serial messages in Ani-Basic language. The command information and serial communication are specified in [53]. For both position and velocity modes, specific trajectory files are created in Matlab that include velocity/position trajectory (e.g. sine wave, square wave), and acceleration information. These trajectories are recorded as text files and read by a C++ code that communicates with the motor in Ani-Basic Language via serial communication at 115200 bps. The commanded position, velocity, acceleration and real-time position, velocity, acceleration values can be read back from the motor controller. Reading the motor values allowed us to validate the gyroscope output and to see whether the ocelli circuit is in desired position or not. To

measure frequency response characteristics, concatenated sine waves are sent as velocity trajectory at different frequencies at velocity mode. To understand the ocellar sensor validity (explained in the next section), step inputs are sent at position mode.

After storing the gyro, ocelli, Vicon^{TM} and raw imagery data in a bag file, post-processing is summarized in Figure 22. Using the raw imagery in the bag file, optic flow field vectors are computed with another C++ code, using OpenCV Lucas- Kanade Algorithm. A text file is generated that includes the time stamps and optic flow x & y vectors for each image. For the other data, the bag file is unbagged and parsed to extract the ocelli, gyro, Vicon^{TM}, motor data and related timestamps. Optic flow vectors generated from Lucas Kanade algorithm are also parsed. The text file contains 60 fps optic flow information. To obtain lower frame rate results, the optic flow values are down-sampled to factors of 60. Since we have data coming from different sources at different sampling rates, synchronization is necessary using a common time vector. A common time vector for all data is created with the lowest sampling time possible, which is the microcontroller sampling time, 0.003 seconds. All data is interpolated using this time vector.

Since the communication modules are developed for embedded platforms, it will not take much effort to transfer this system to on-board computers used on quadrotor helicopters (quadcopters) through Secure Shell (SSH). The time synchronization can be carried out with firmware that force one computer's clock to follow another one (e.g. 'chrony' synchronization for ROS).

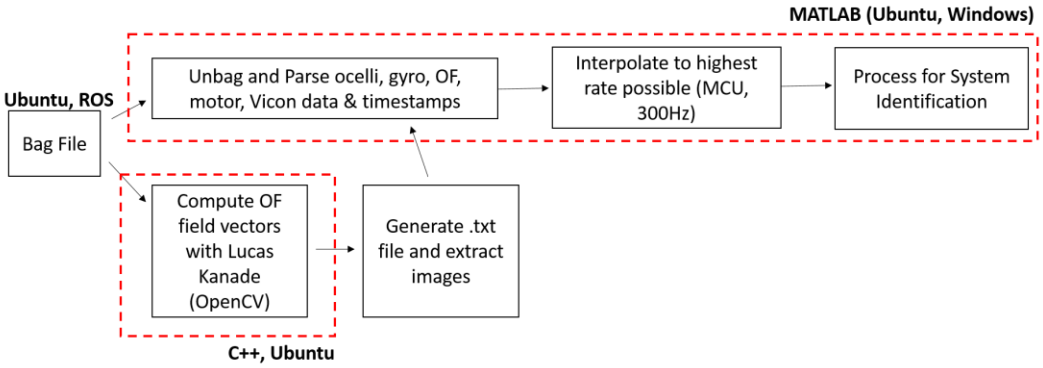

Figure 22: Post-processing block diagram: Optic flow vectors are computed and extracted as a text file. The bag file is parsed, interpolated and processed for data analysis.

Magnitude-Squared Coherence

The spectral coherence is a measure that can be used to examine the relation between two signals (or data sets). It is commonly used to estimate the power transfer between the input and output of a linear system. The magnitude-squared coherence between two signals x(t) and y(t) is defined as:

$$C_{xy}(f) = \frac{|G_{xy}(f)|^2}{G_{xx}(f)G_{yy}(f)} \quad (39)$$

Where $G_{xy}(f)$ is the cross-spectral density between x and y, and $G_{xx}(f), G_{yy}(f)$ are the auto-spectral density of x and y, respectively. If the signals are ergodic (statistical properties can be deduced from a sufficiently long process) and the system function linear, the magnitude-squared coherence function estimates the extent to which y(t) may be predicted from x(t) by an optimum linear least squares function [92]. The transfer functions and operations described for mathematical model of the system itself and ocellar sensor transfer characteristics are linear. Thus, we expect the system to be linear. The magnitude-squared coherence is added to the frequency response plots as a performance parameter showing linearity.

For an ideally linear system:

$$y(t) = x(t) * h(t) \leftrightarrow Y(f) = X(f)H(f) \quad (40)$$

$$G_{yy}(f) = |H(f)|^2 G_{xx}(f) \quad (41)$$

$$G_{xy}(f) = |H(f)|^2 G_{xx}(f) \qquad (42)$$

$$C_{xy}(f) = \frac{|H(f)G_{xx}(f)|^2}{G_{xx}(f)G_{yy}(f)} = \frac{|H(f)G_{xx}(f)|^2}{G_{xx}(f)^2|H(f)|^2} = 1 \qquad (43)$$

Where $h(t)$ is the impulse response and $H(f)$ is its Fourier Transform.

Values of coherence satisfy $0 \leq C_{xy}(f) \leq 1$. If there is perfect linear relationship between x and y at a given frequency, $C_{xy}(f) = 1$. If C_{xy} is less than one but greater than zero, it is an indication that either noise is an inherent component of the system measurement, that the assumed function relating x(t) and y(t) is not linear, or that y(t) is producing output due to input x(t) as well as other inputs. If the coherence is equal to zero, it is an indication that x(t) and y(t) are completely unrelated.

In physical world, a perfect linear relationship is rarely realized. In practice, coherence values higher than 0.5 are acceptable for testing linear systems. For the experiments below, the coherence values dip down at specific frequencies, around 1-2 Hz, for all measurements. Although the input sine waves includes these frequencies, it is believed that the motor was not successful at implementing these frequencies. All of the final measurements include coherence values higher than 0.5, to be in a practically acceptable region.

Ground Truth

The first consideration for ground truth was the Vicon™ motion detection system. However, its cameras strobe at frequencies 50-100Hz and use reflected infrared light that is strobed from a ring of LEDs surrounding each camera. The band-pass filter circuit is able to pick up these frequency components of the infrared light, resulting in the corruption of the output signal. Alternative ground truth options are the velocity readout from the servo motor controller and the gyroscope sensor. To choose one as ground truth, a chirp signal between 0.1 to 10 Hz was given to the motor as velocity input and the comparative responses of motor velocity readout and gyroscope were verified, with respect to the Vicon™ system as input. The ideal response should be a flat curve. As seen in Figure 23,

the gyroscope provides a more flat magnitude very close to 0 dB, and less phase delay than motor velocity. The magnitude-squared coherence plot indicates a linear input-output relationship at an existing frequency. The gyroscope coherence is higher than motor velocity across all test frequencies, therefore, it is is regarded as ground truth for further analysis. The curves are shown up to 15 Hz to show the coherence decay outside the test frequencies.

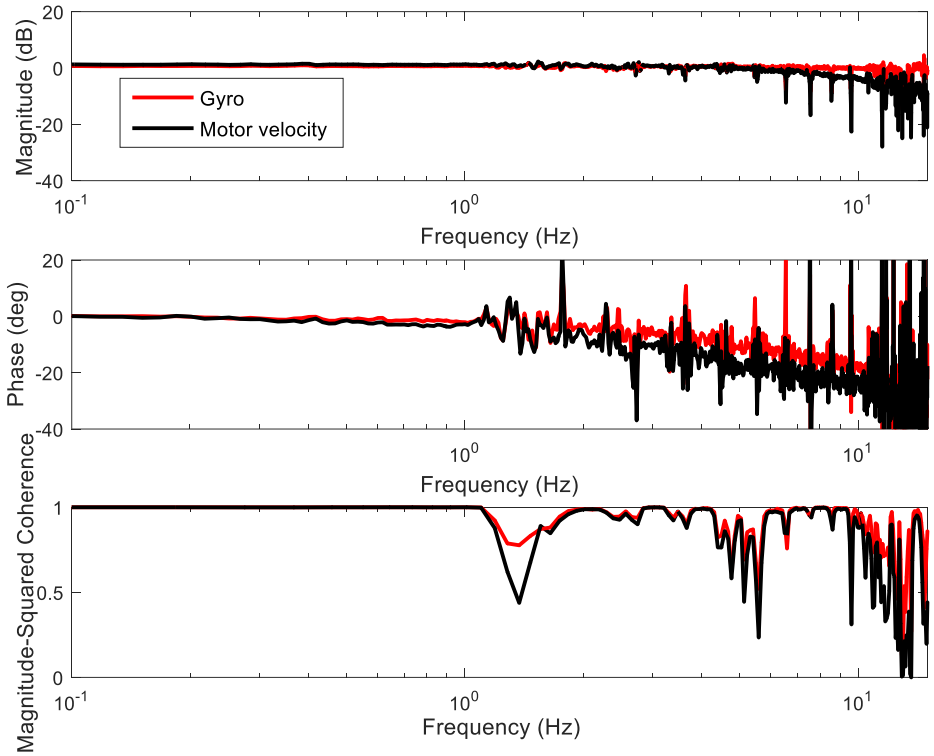

Figure 23: Motor velocity and gyro frequency response, as seen by Vicon™ motion detection system as input: Frequencies after 10 Hz were shown to prove the decrease in coherence out of controlled motion frequencies. Gyroscope shows a flatter magnitude response and higher coherence than motor velocity, therefore it was chosen to be the ground truth.

Understanding Ocellar Sensor 'Valid Range'

The ocelli circuit is assumed to work under a specific luminance pattern to be an angular rate sensor. Assuming a bright sky and dark ground, when the photodiodes are looking to the sides, each of them

see a different horizon. One photodiode sees a brighter patch, while the other one sees a darker patch. For this algorithm to work, the luminance gradient from the sky to the ground should be constant and negative. We use a light source with a diffuser to create this artificial sky and horizons. The diffuser prevents the DC source from acting as a point source, by helping to distribute the light intensity along the diffuser surface. This way, light source acts as the sky, rather than the Sun. The photodiodes should see the two edges of the source as two horizons. This way, when a rotational motion is applied, brighter-darker patch assumption will be satisfied. The photodiodes should be bent towards the source to intersect their field of views. To understand whether an intersection is created, the azimuthal position of the motor is varied and the photodiode outputs are checked if they share an overlapping field of view. Figures 24 and 25 show the unbent and bent raw photodiode outputs, with respect to the azimuthal position of the motor. A partially overlapping field of view was achieved by bending the photodiodes towards the light source.

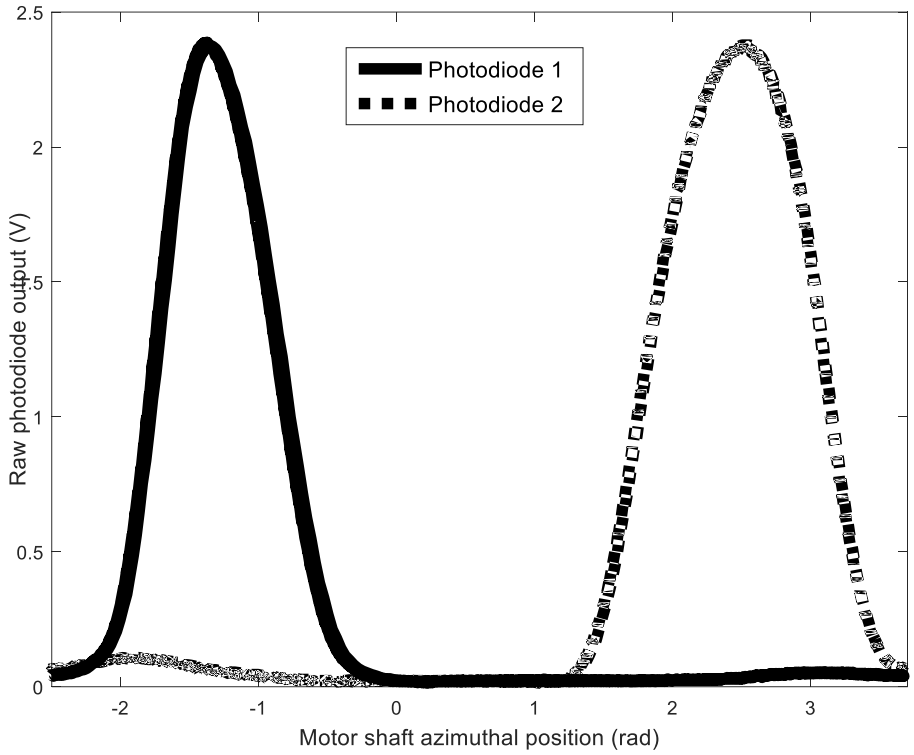

Figure 24: Unbent photodiode output vs. motor shaft azimuthal position: Photodiode outputs increase as they pass by the light source. Field of views are not overlapping.

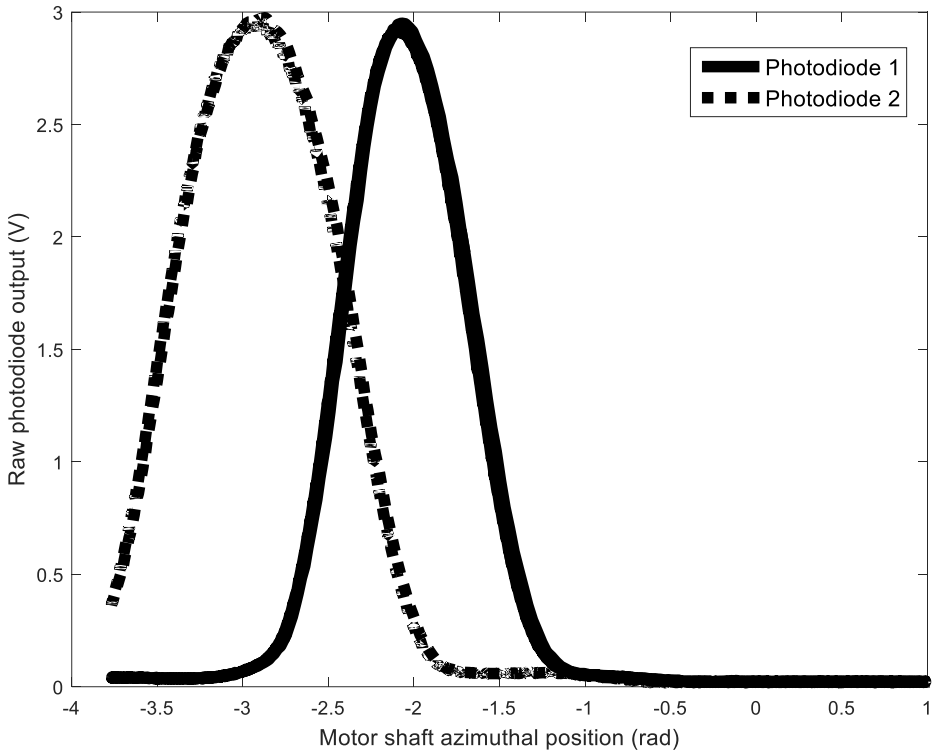

Figure 25: Bent photodiode output vs. motor shaft azimuthal position: Photodiode field of views are partially overlapping, which is required for the ocellar sensor to work. In this (incorrect) configuration, there are angles where simulated roll motions do not produce any change in the photodiode outputs.

Due to the small size of the light source and small field of view of the photodiodes (around 90° each), the maximum swing of the motion stimulus needs to be small enough to ensure that the photodiode outputs are changing symmetrically with respect to each other. To understand the dynamic range circuit's velocity, the azimuth was varied with small steps. For each position value, a target velocity was given to the motor and the circuit output was compared to the gyro output. For the region outside the light source dominance, the circuit outputs are not reliable.

Figure 26 shows a valid region (azimuthal position changes from -0.2 to 0.2 radians). In this range, photodiode outputs are symmetric to each other and the ocelli output directionally matches the gyro output.

Figure 27 shows an invalid region (azimuthal position changes from -1.4 to -0.2 radians). In this range, photodiode outputs are not symmetric to each other. Ocelli is not in agreement with gyro. Using this data, the maximum displacement for the ocellar circuit is determined to be 1 radian. All of the following characterizations are done in this valid region.

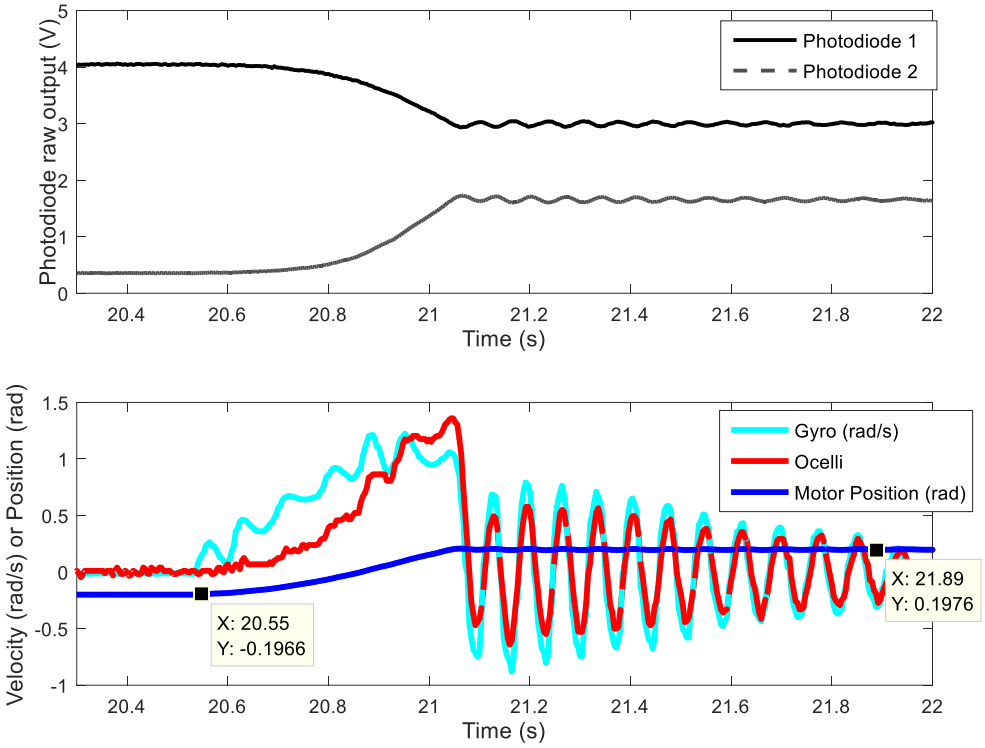

Figure 26: Ocelli in valid range: (Above) Symmetric photodiode raw output. (Below) Gyro and ocelli output for motor azimuthal position (-0.2 to 0.2 radians). Ocelli output is in agreement with gyro in this range.

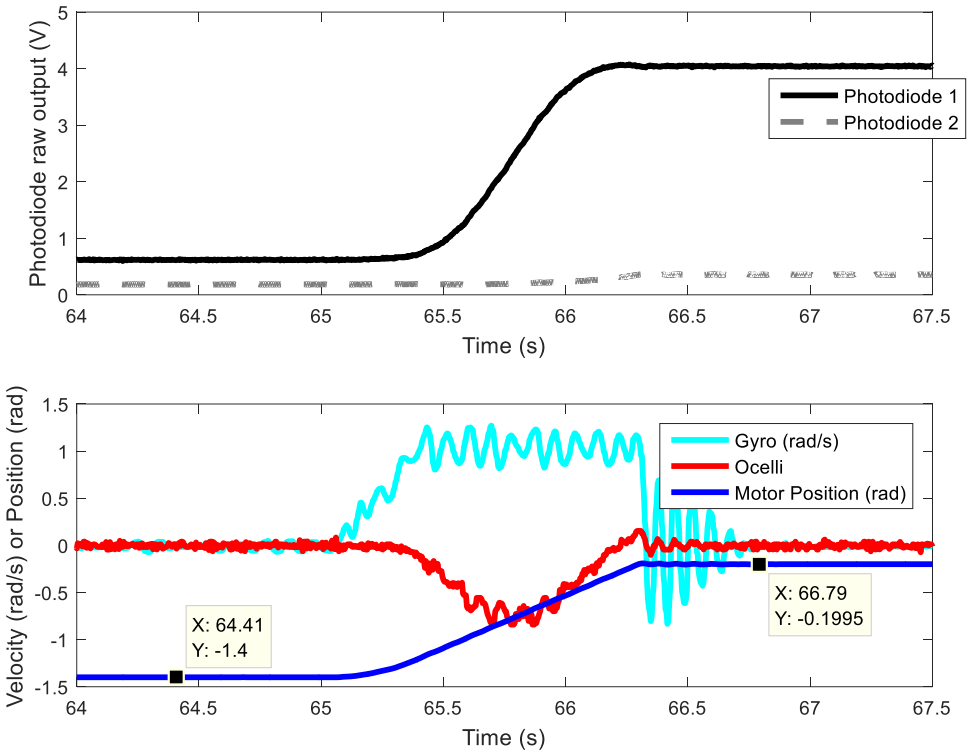

Figure 27: Ocelli in invalid range: (Above) Asymmetric photodiode raw output. (Below) Gyro and ocelli output for motor azimuthal position (-1.2 to 0.2 radians). Ocelli output is not in agreement with gyro in this range.

Ocellar Sensor Frequency Characterization

Frequency characterization is done in two ways. First, to confirm the proper operation of the band-pass circuit, the raw photodiode output is used as input and filtered signal is used as output. Although the band-pass circuits can operate up to higher frequencies, the motor stimulus is limited to 10 Hz, only 0.1-10Hz data is obtained for circuit's motion characterization. To demonstrate that the photodiode and band-pass filter combination can operate at higher frequencies, an LED was driven by a signal generator between 3-100 Hz.

A second frequency characterization was done to compare the optic flow and ocelli outputs with the gyro as ground truth.. This provided us with information about how well the sensors operate within the motion frequencies, in comparison to each other with the same inputs.

Circuit Frequency Characterization

A chirp signal is given as a motor velocity command. Figure 28 shows the simulated circuit output, Figures 29 shows the right and left circuit frequency responses. Between 0.1-10Hz, the circuit simulation shows 20dB/decade increase in magnitude, starting from -38dB to 1 dB. The phase delay starts from -90 degrees and reaches to -125 degrees at 10 Hz. The data from both photodiodes show the similar response. Right circuit magnitude starts from -38dB and reaches to -2dB. Left circuit starts from -38dB and reaches to 0dB. Phase response reaches to -140 and -124 degrees for right and left, respectively, after starting from -90 degrees.

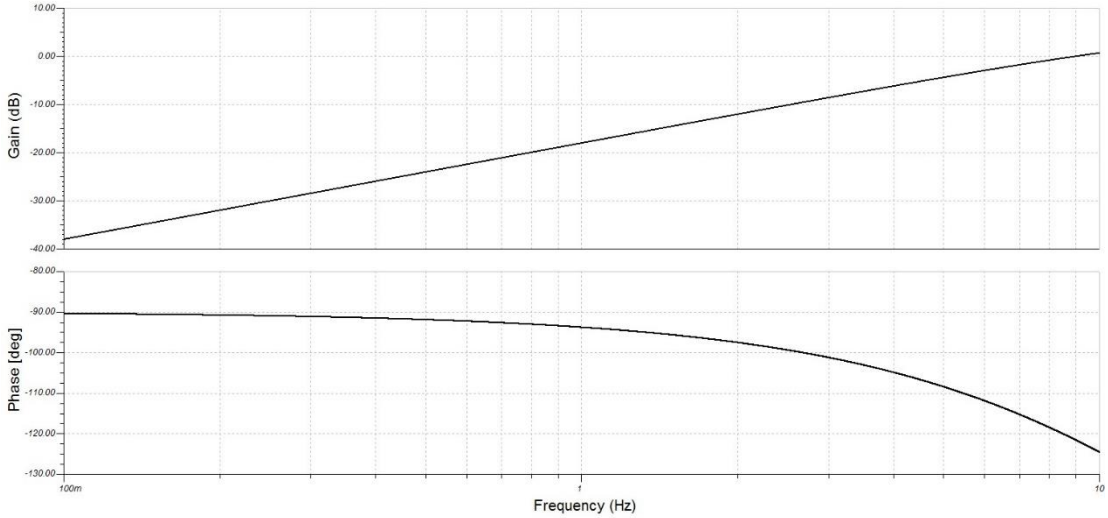

Figure 28: Band-pass filter simulated AC transfer characteristic between 0.1-10 Hz: Magnitude increases with 20 dB/decade. Phase drops from -90^0 to -125^0 at the end of 10 Hz.

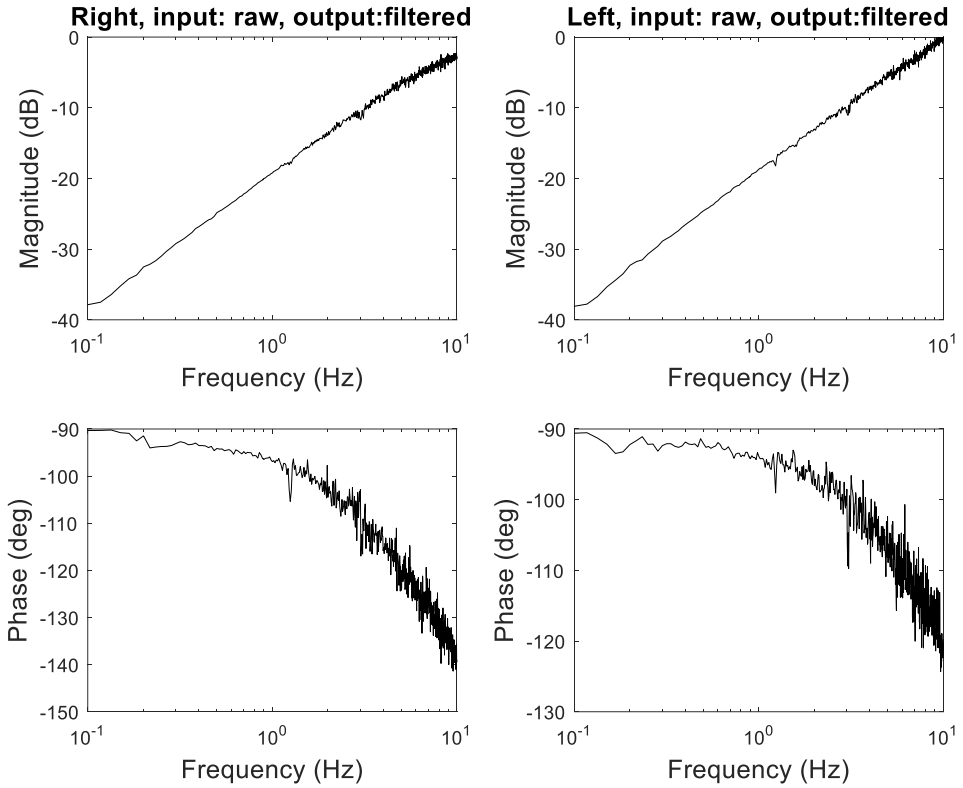

Figure 29: Right and left band-pass filter measured AC transfer characteristics between 0.1-10 Hz: Magnitude and phase plots are in agreement with simulation (Figure 28).

To demonstrate that the photodiode and band-pass filter combination can operate at higher frequencies, an LED was taped to one photodiode (See Figure 30). Electrical signal (sine wave, voltage-controlled) from signal generator is swept between 3-100 Hz. Figure 31 shows the AC characteristics simulation between 3-100 Hz. The gain starts from -8.59dB and reaches to 5.6dB at 50 Hz, then it decreases to 4.74dB at 100 Hz. The phase starts from -101 degrees at 3 Hz, decreasing to -205 degrees at 100 Hz. Figure 32 shows the frequency response of the circuit from the photodiode input from LED to the filtered output. The magnitude response starts from -10.25 dB and reaches to -0.29dB at 50 Hz. Then it decays to -1.281dB at 98.6 Hz. The phase response starts from -105.8 degrees at 3 Hz, decreasing to -180.5 degrees at 98.76 Hz. Qualitatively, circuit simulation is close to actual data. Circuit simulation

results in 103 degrees phase delay, data results in 75 degrees phase delay. The circuit gain increases by 14 dB up to 50 Hz, real data gain increases by 10 dB.

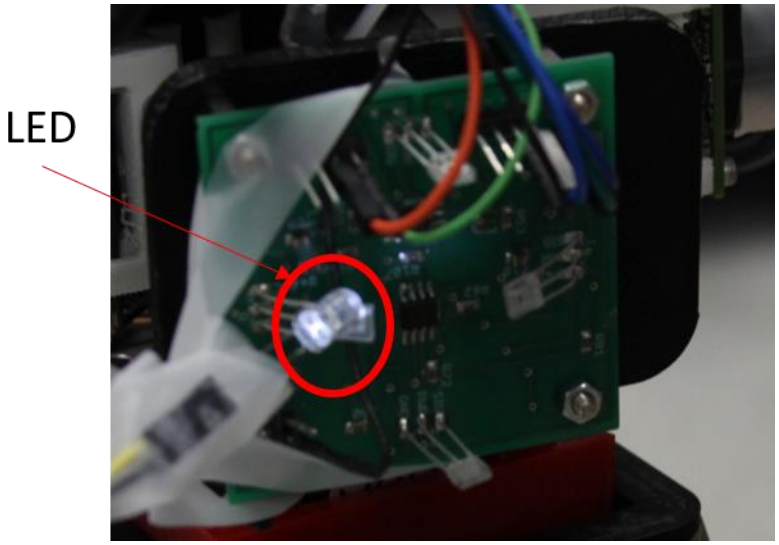

Figure 30: LED sweeping: LED was taped to photodiode and power supply signal is swept between 3-150 Hz.

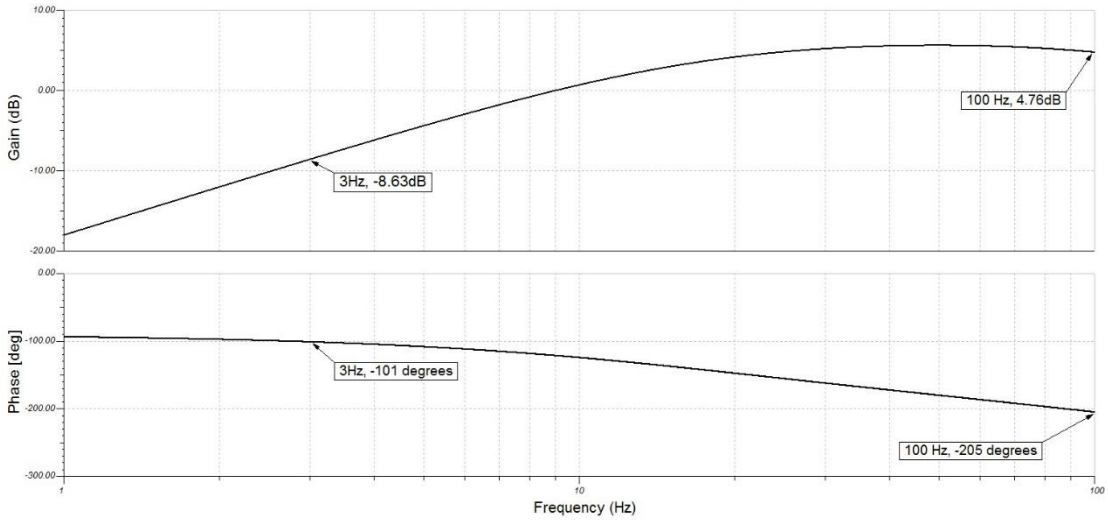

Figure 31: Right and left band-pass filter simulated transfer characteristics between 1-100 Hz: Simulation is shown to compare with LED sweeping results in Figure 32.

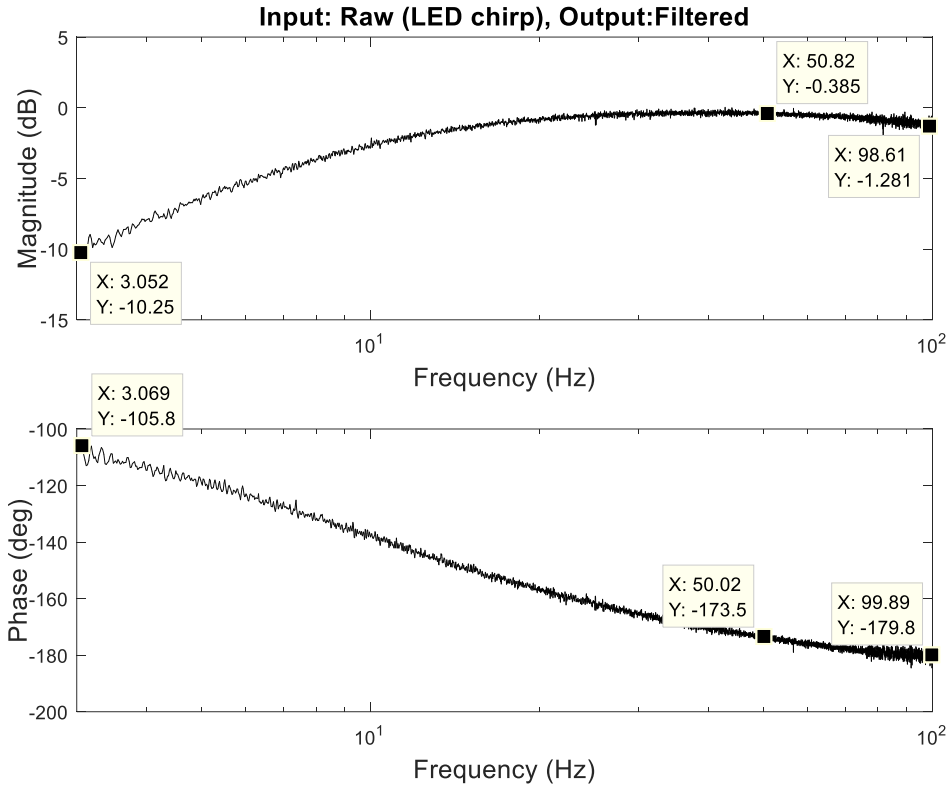

Figure 32: Right band-pass filter measured transfer characteristics in response to LED chirp between 3-100 Hz: Magnitude increases 20 dB/decade. Phase drops from -105^0 to -180^0. (In agreement with simulation in Figure 31).

Sensor vs. Ground Truth Frequency Characterization

To characterize ocellar sensor frequency response with respect to the gyroscope (acting as the ground truth velocity), concatenated sine waves were given as velocity input. The operation was performed in the valid angle range described above. The ocelli output is a voltage value. Its magnitude is scaled to match with gyro. This frequency response is from gyroscope as input, to the full ocellar sensor as output. Within the test frequencies, the ocellar sensor shows a relatively stable magnitude around 0 dB. The phase response is degrading over the frequency range. Figure 33 shows the ocellar sensor frequency response. Between 0.1- 1 Hz, there is almost no phase delay between ocelli and gyro. After 1 Hz, ocelli shows a phase delay of approximately 15 degrees. The data after 10 Hz was not taken into account, since the input stimulus cannot exceed 10 Hz. The components at higher frequencies are due

to mechanical noise inherent in the motor. Coherence dips are happening at the same frequencies with the other experiments, therefore it is believed that the motor was not able to implement those frequency components. Ocelli always shows a coherence above 0.5, which is practically acceptable.

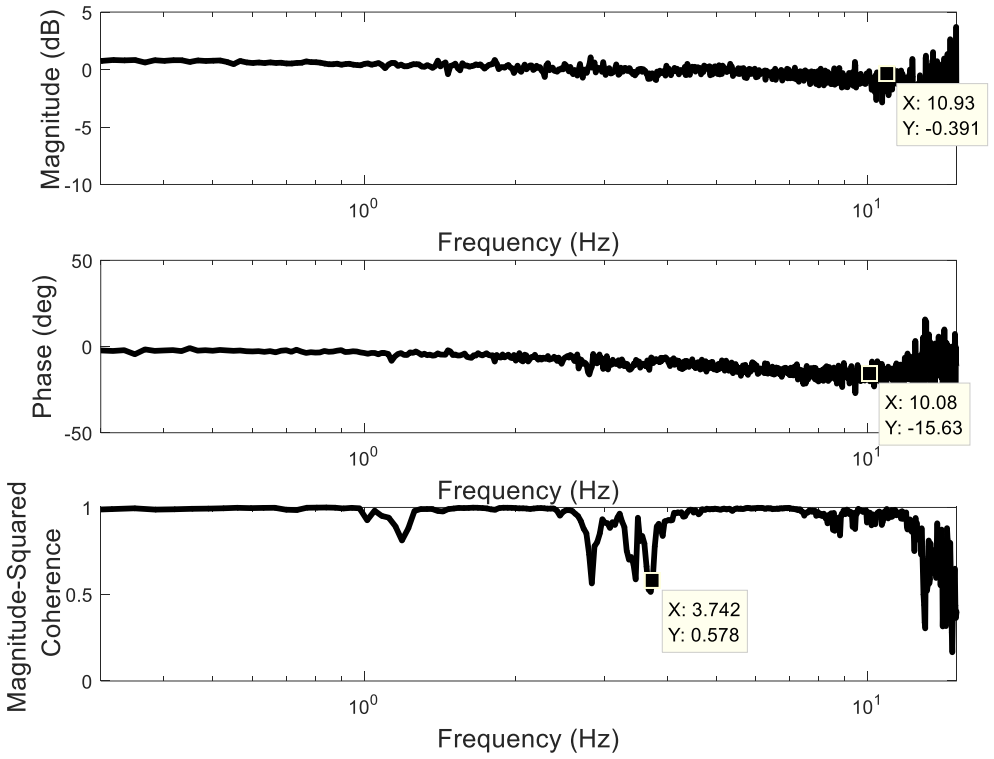

Figure 33: Ocelli frequency response with respect to gyro as input: Frequencies after 10 Hz were shown to prove the decrease in coherence out of controlled motion frequencies. Ocellar magnitude is relatively flat, showing around 1dB difference from beginning to end. Phase delay reaches to -15^0 at 10 Hz.

Optic Flow Frequency Characterization

Figure 34 shows the time-domain signals comparing gyro, ocelli, and optic flow in 0.5Hz, 1Hz, 5Hz and 10 Hz windows, respectively. The outputs of optic flow and ocelli are scaled to match gyro output (rad/s) at each window. The ocelli and optic flow are in agreement with gyro signal at each frequency window.

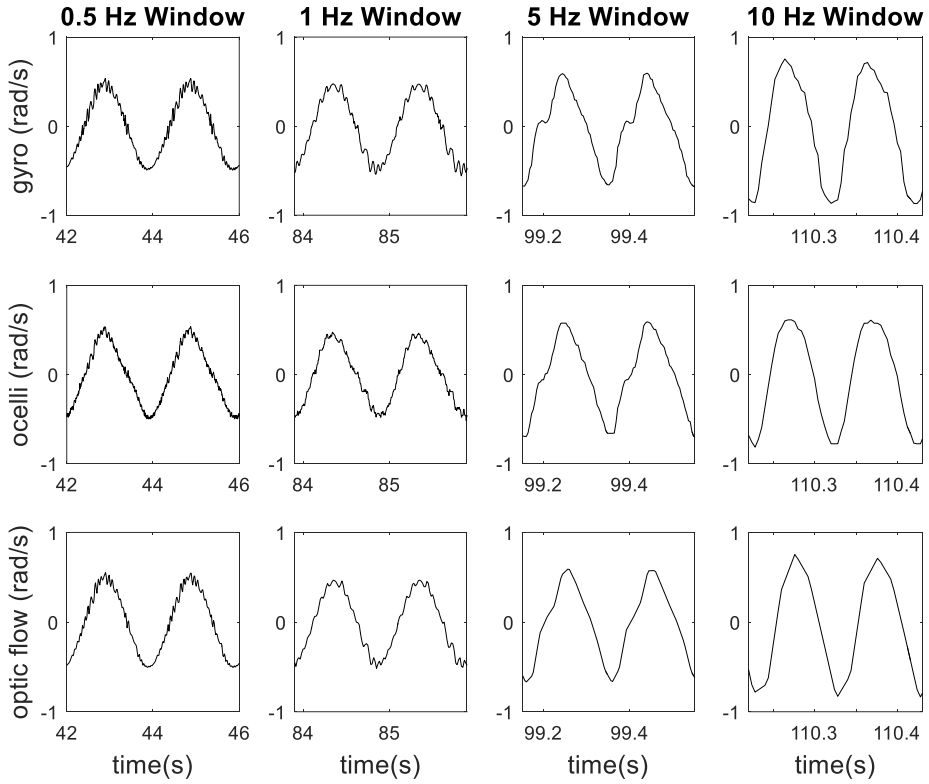

Figure 34: Time signals of gyro, ocelli and optic flow in 0.5, 1, 5, 10 Hz windows: All sensor outputs are scaled to match gyro (rad/s) at each window.

Figure 35 shows the optic flow frequency characterization for 60 fps data, using Lucas- Kanade with 25 pixels window size and 16 feature points (4*4). The entire magnitude response is very close to flat. There is almost no phase delay until 1 Hz, then it reaches to -35 degrees at 10 Hz. Taking into account that this optic flow data is obtained with the highest frame rate, the magnitude response is expected to degrade as the frame rate decreases. Although the optic flow frequency response remains approximately flat with these settings, the frequency response is related to the motion algorithm, frame rate and window size, as will be seen next. Varying these parameters, a worse high-frequency response will be obtained, which is the real-life case with flying vehicle on-board computers. All in all, this data shows the maximum bandwidth the optic flow can achieve within the test limitations.

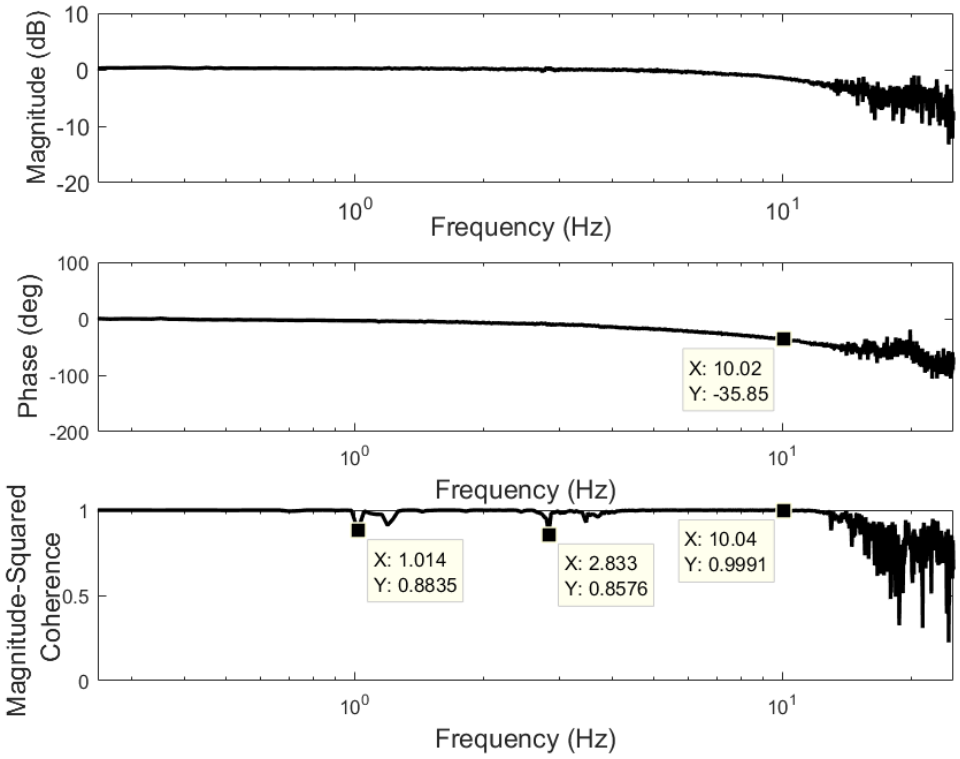

Figure 35: Frequency response of optic flow with respect to gyro as input: Overall magnitude decrease is 1.42dB. Phase delay reaches to -35^0 at 10 Hz.

Ocellar Sensor – Gyro Voltage-Velocity Mapping

To understand the expected ocelli output (in volts) for a given gyro (rad/s) value. The data for ocelli and gyro across 1-10 Hz test frequencies was combined. With 0.005 rad/s intervals, expected ocelli output (V) and gyro (rad/s) values were calculated (16 data points for both). These points were fitted to a line of equation

$$f(x) = p1 * x + p2 \quad (44)$$

where $p1 = 0.164$ and $p2 = 2.489$, R^2=0.9902. Figure 36 shows the mapping plot. It shows that the ocelli output is monotonically increasing with increasing gyro amplitude, implying linearity. The

standard deviation (error bars) are big because of the discretization limit of the ADC. ADC has 4.8mV resolution, the overall motion is within 140 mV.

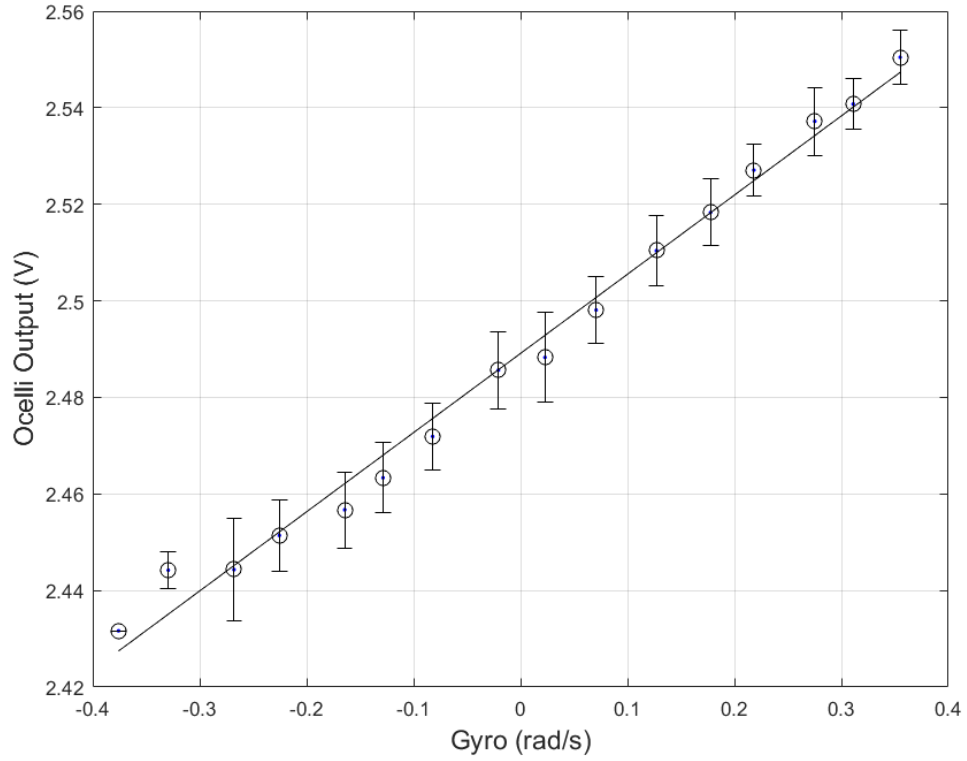

Figure 36: Ocelli - gyro mapping plot. It shows the expected ocelli output (V) for a given gyro measurement (rad/s). Ocelli output is monotonically increasing with increasing gyro values. (The leftmost error bar is very small, not visible as compared to others).

Performance-Related Parameters

Frame Rate

Frame rate is the frequency at which the camera displays consecutive images. From equation 2, Lucas-Kanade algorithm extensively uses spatial and temporal derivatives, using numerical differentiation. To give an example, let f be a given function that is only known at a number of isolated points. The

problem of numerical differentiation is to compute an approximation of the derivative f' of f by suitable combinations of the known values of f.

Assuming that function f is differentiable, the derivative f'(a) for some real number a is defined as:

$$f'(a) = \lim_{h \to 0} \left(\frac{f(a+h) - f(a)}{h} \right) \quad (45)$$

For very small h, this derivative can be approximated by:

$$f'(a) \approx \frac{f(a+h) - f(a)}{h} \quad (46)$$

This approximation involves error and this error increases as h increases. To demonstrate this, one can use f(x)=sinx, f'(x)=cosx and compute the error between f'(x)=cosx and f'(x)~ $\frac{f(x+h)-f(x)}{h}$. The error will increase as the h values increase.

Figure 37 shows the frequency response of 60, 30 and 20 frames-per-second (fps) optic flow results from gyro as input and optic flow as output. As frame rate decreases, optic flow magnitude response rolls off steeper and reaches to -2.64, -4.92 and -9.62dB at 10 Hz for 60, 30, and 20 fps, respectively. For all frame rates, the phase delay remains constant. For 0.1-1.1 Hz, there is almost no phase delay between optic flow and gyroscope. After 1.1 through 10 Hz, the phase delay increases and reaches to -35 degrees. The coherence of 20 fps measurement is the worst, increasing frame rate increases the coherence as well.

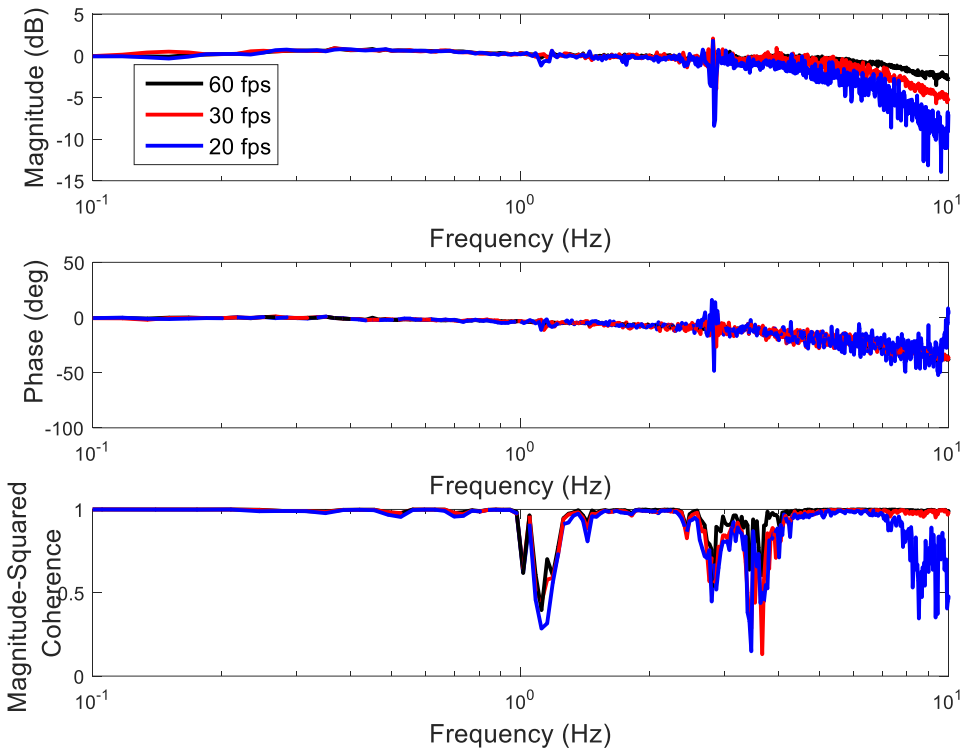

Figure 37: Optic flow frequency response with different frame rates, as seen by input gyro: As the frame rate decreases, roll-off at higher frequencies is steeper. Higher frame rate results in better coherence. Phase delay does not change due to frame rate.

Besides numerical differentiation error, another explanation lies under the Taylor series approximation used to derive the motion constraint equation. Taking only the first order components assumes that the change in motion is small. However, when the change is larger, the second order components will come into play and the motion constraint equation will no longer hold. When the motion is too fast for a given frame rate, the spatial/temporal estimate assumption breaks down. In practice, this resulted in an optical flow measurement of erroneously low magnitude.

Aliasing is another way to look at this roll-off. When the frame rate decreases, there are less optic flow vectors to sample the given sine wave. These vectors may be computed at random points of the

sine wave, not exactly catching the peak amplitudes. If the frame rate is higher, more optic flow points will result in a more accurate sine wave, catching the peaks.

[54] studies the optic flow outputs as the angular rate changes. According to their findings for two different optic flow algorithms, optic flow matches with real rate for slow motions, for a specific resolution. As the rate increases, optic flow cannot capture images often enough to get an accurate estimate of angular rate. Optic flow first draws a unity line with real rate, then this line starts showing a fixed rate, then it rolls completely off to zero.

To overcome this, one may increase the frame rate, or, use a smaller image (e.g. binned by 2) to double the frame rate. With the current setup, 752*480 pixels image can go up to 20 fps. When the image is binned by 2, the frame rate increases to 60 fps for 376*240 pixels image. This solution will result in losing maximum image resolution.

Window Size

Lucas- Kanade algorithm assumes that the motion is the same for all pixels in a window of w by w pixels. This tracking window size determines the number of equations (hence optic flow vector candidates) to be used in the least squares method. Assuming constancy in motion, more optic flow vectors will give more data points to determine the best fit for optic flow. However, if the window is too large, a point may not move like its neighbors.

Figures 38 and 39 show the window size vs. the optic flow frequency response. Changing window sizes significantly affected the coherence plot. Phase delay remained the same for all window sizes. Magnitude is the most erroneous for 10 and 20 pixels (10*10, 20*20) window size, however it stays relatively the same for the rest. The coherence is the worst using 10 pixels. It improves as the window size increases from 20 to 40 pixels, remains the same after 40 pixels through 70 pixels.

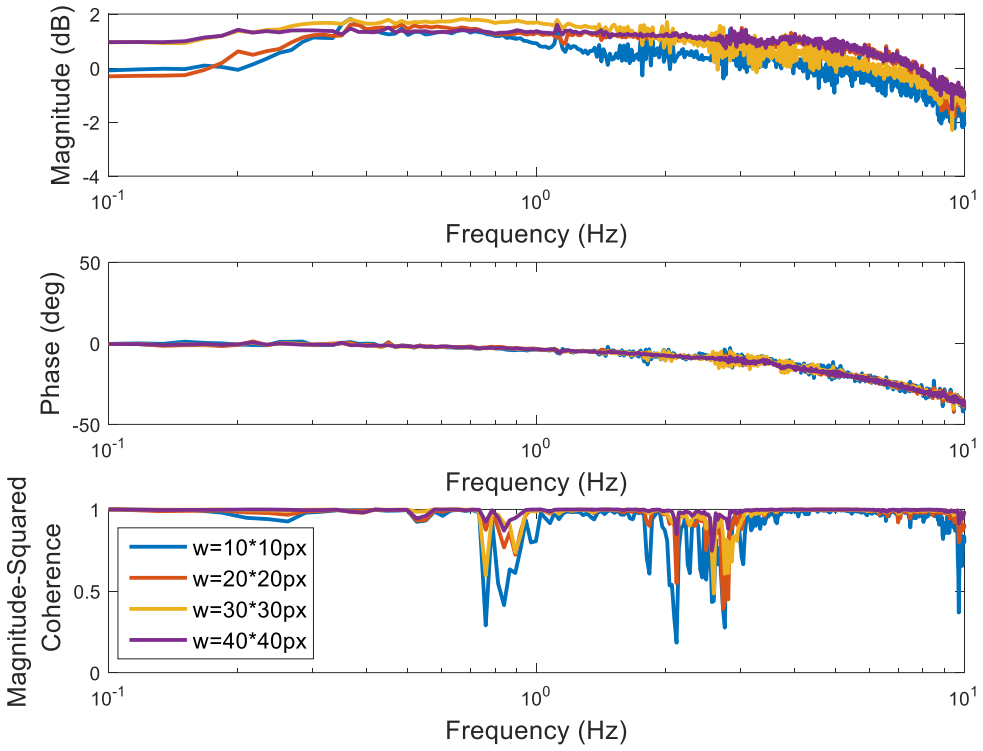

Figure 38: Optic flow frequency response with different window sizes (w=10,20,30,40), as seen by input gyro: Very small windows (10*10px) result in erroneous magnitude response. Magnitude response and coherence improves as window size increases, phase delay remains the same.

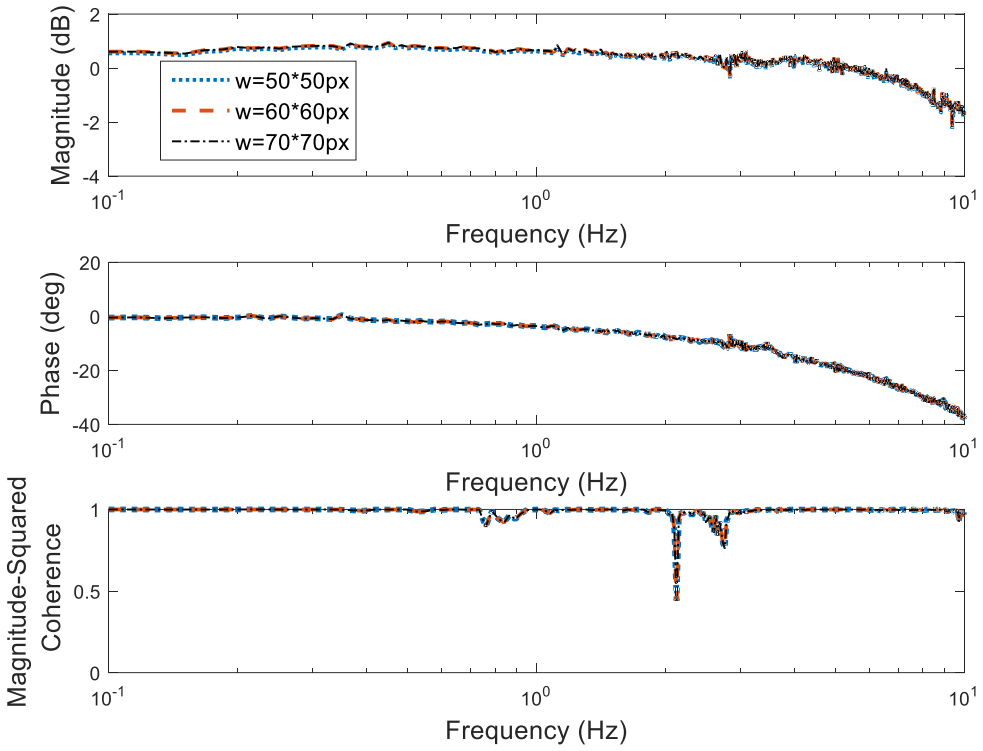

Figure 39: Optic flow frequency response with different window sizes (w=50, 60, 70), as seen by input gyro: After 50*50px window, magnitude, phase, and coherence plots do not change.

Feature Points

Feature points are the number of center pixels located on each image. Around these center pixels, optic flow vectors are calculated within the window size. The number of feature points determines the number of optic flow vectors computed. The plotted optic flow is only the x component of average optic flow field. The feature points are equally distributed over x and y dimensions of the image. The spacing between them is:

$$x\ (or\ y) spacing = \frac{image\ width (or\ height)}{number\ of\ feature\ points\ along\ x\ (or\ y)} \quad (47)$$

x feature points are referred to as x-by-x center pixels. Figures 40 and 41 show the image scene with 10-by-10 and 4-by-4 feature points, respectively.

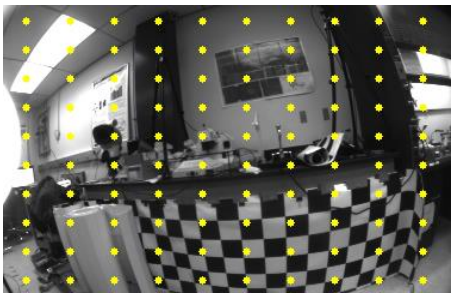

Figure 40: Camera scene (10*10 feature points).

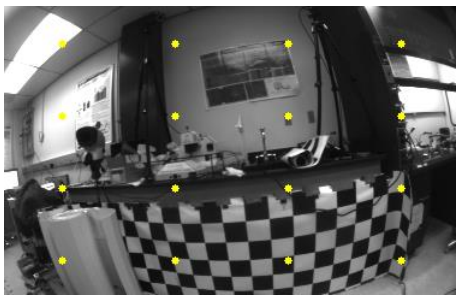

Figure 41: Camera scene (4*4 feature points).

Figure 42 shows the optic flow frequency response with respect to different number of future points. 2-by-2 feature points result in the most erroneous optic flow magnitude. The magnitude response improves after 2-by-2 and stays relatively the same from 4-by-4 to 15-by-15 feature points. Similar to window size result, the change in phase remains the same between feature points. The coherence is the worst using 2-by-2 feature points. Increasing the feature points improves the coherence, however coherence remains the same after 8 feature points. This means that sufficient number of optic flow vector data points are accumulated to make the best fit for optic flow with 8*8 feature points. More feature points bring redundant data points.

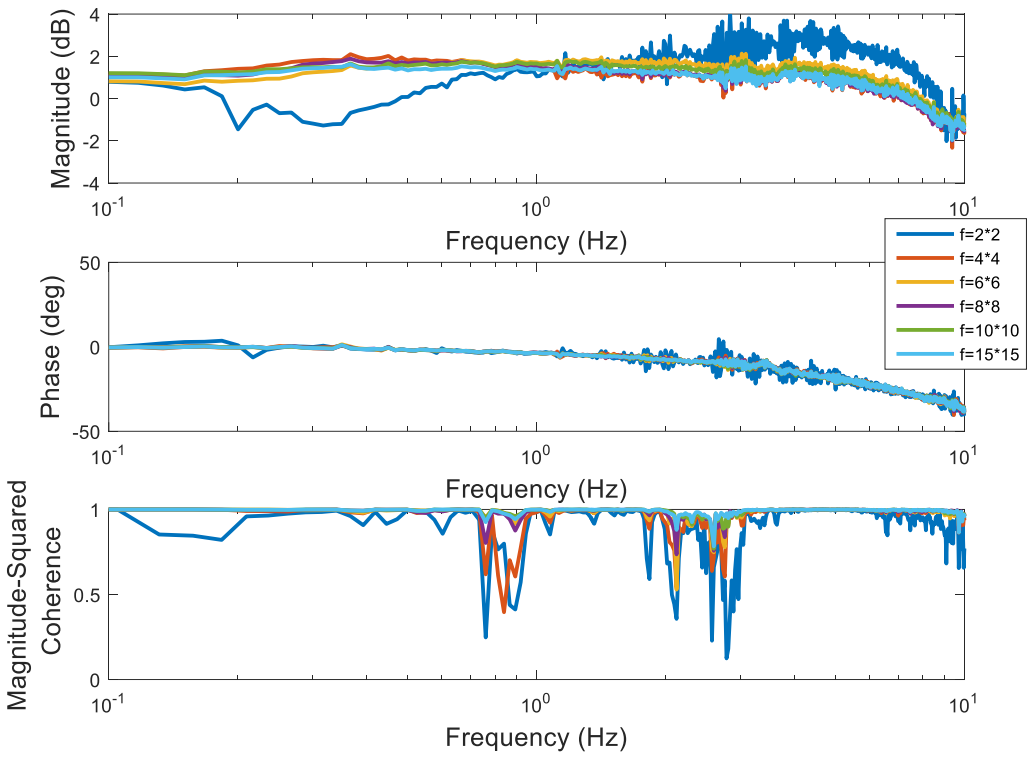

Figure 42: Optic flow frequency response with different number of feature points (f), as seen by input gyro: 2*2 feature points result in erroneous magnitude plot. As the feature points increase, magnitude and phase plots do not show much change, however coherence improves.

Luminance Intensity

DC light input power is varied to understand how the luminance intensity changes the ocellar circuit output. The circuit outputs at the same frequency were compared. Figure 43 shows the peak-to-peak amplitudes with respect to input power, for 10 Hz motion. As the power increases, amplitude increases, as expected. The fitted line has coefficients of p1=0.088, p2=0.006. This brings a necessity for ‘adaptive gain’ for different luminance values in the environment.

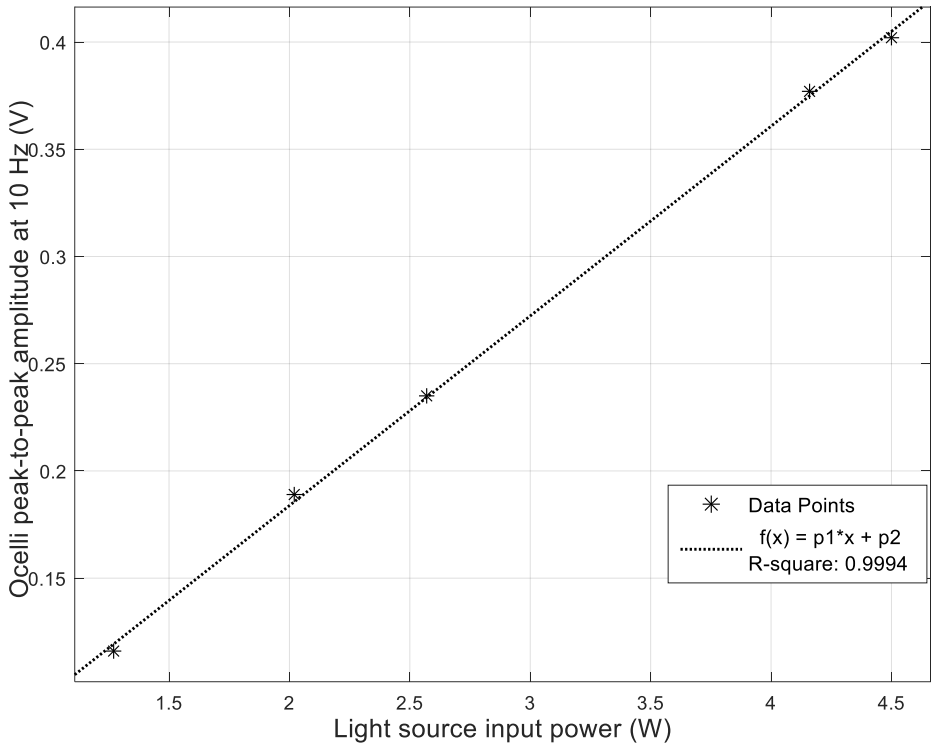

Figure 43: Light source input power vs. ocelli peak-to-peak amplitude: Luminance increase linearly increases the peak-to-peak amplitude. DC light source is specified in Table 3.

Photodiode Bending

The photodiodes should be bent towards the light source to share an intersecting field-of-view (FOV) and to satisfy that one's output is increasing while the other's is decreasing. The bending determines how much their field of views intersect and how much they are seeing the edges of the light source as two different horizons. The reference for bending is seen in Figure 44. If $\beta=0^{o}$, no common luminance is shared. If $\beta=90^{o}$, their field of views completely intersect and no symmetric change with respect to each other is observed. Assumption is satisfied for β values between 0-45^{o}, specifically $\beta=30^{o}$, 40^{o},45^{o} raw outputs are observed to be symmetric to each other. For $\beta\sim90^{o}$, same sine wave shape is seen at the same instant.

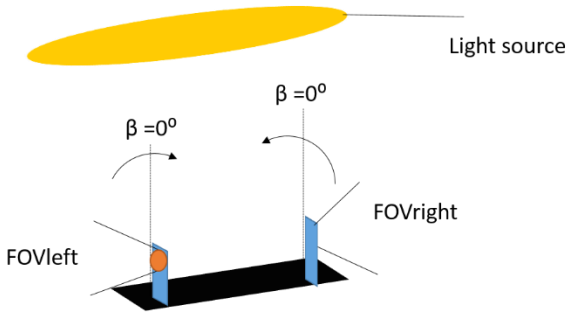

Figure 44: Bending illustration: The photodiodes should share an intersecting field-of-view (FOV) towards the light source for the sensor to operate. Bending values $30^0<\beta<45^0$ were observed to give symmetric photodiode outputs. $\beta=90^0$ completely overlaps the field of views, without distinct horizons for each photodiode.

Test Setup Limitations

The maximum motion frequency achieved with the motor is around 10 Hz for velocity mode. For position mode, the frequency is even lower, 2 Hz. Above these frequencies for related modes, the motor does not follow the input position/velocity. The higher frequency components in the plots are from inherent mechanical vibrations of the motor, and the flickering of laboratory lights at 60 Hz or its harmonics at 120-180Hz. The camera used has a theoretical claim of 87 fps frame rate. However, when this frame rate is used, frame drops are observed. Optic flow calculation is highly corrupted by frame drops. Frame drops were minimized with 60 fps frame rate.

Also, using two cameras for covering more field was the first try. This configuration needs triggering to satisfy that the cameras are taking photo at the same time. Triggering was achieved with two PX-4 Inertial Measurement Units working as master and slave. However, data transfer limitation from USB port brought lower frame rate problem again, hence frame drops stopped after switching to one camera, at the same frame rate. To allow for triggering, frame rate had to be decreased to 20 fps, which limited the optic flow bandwidth. To show the maximum achievable bandwidth for optic flow with this configuration, only one camera is used with 60 fps, 376*240 pixels image.

Chapter 4: Sensor Fusion

As described in chapter 3, ocellar sensor shows a relatively stable magnitude across the test frequencies. Optic flow frequency response can keep up with the ocellar sensor for 60 fps data. As the frame rate decreases, optic flow magnitude plot rolls off. At high motion frequencies (where the optic flow information degrades), it is possible to use the ocellar circuit. This chapter first presents the biological background for sensor fusion in insect compound eyes and the ocelli. Then the general fusion approaches from the literature are discussed. Finally, the optic flow and the ocellar sensor data are fused to demonstrate the high-frequency roll-off compensation of optic flow, using the ocellar sensor.

Biological Background for Sensor Fusion

From the behavioral studies, ocelli and compound eyes are thought to work together for flight stabilization abilities, [21, 23, 25]. In blowfly, it is previously studied that lobula plate tangential cells estimate the self-motion by taking local motion information from compound eyes. One of the cells that are reported to respond optic flow information is a tangential cell, called V1 [55]. [56] reports that V1 responds to ocelli stimulus as well. The response increases with the rate at which the light intensity changes, implying that V1 might be encoding angular velocity information, as well as optic flow information. [57] experiments that a prominent descending neuron called DNOVS1 receive input from two sources: From the photoreceptors of compound eye via large-field motion sensitive cells, and from photoreceptors of ocelli via ocellar interneurons. [58] reports that lobula plate neurons combine inputs from both ocelli and compound eyes. Ocellar responses encode information in three axes, whereas, compound eyes encode in nine. This reveals that ocelli are only able to detect rotation around three axes, thus less specificity with respect to compound eye. If we assume a direct summation of ocelli and compound eye neuronal signals, this might help the flight behavior in three axes (since there will be more information for three axes, from both compound eyes and ocelli). However, for the other six axes, ocelli might output ‘zero’ and the fused response from both compound eye and ocelli might

degrade the flight behavior, which seems like counterintuitive. [58] suggests that each VS neuron is tuned to the ocellar axis closest to its compound eye axis, combining the speed of ocelli with the accuracy of compound eyes, without compromising either.

Having said that ocelli are faster than compound eyes, what is the quantitative difference between these latencies? The response latency depends strongly on experimental parameters, such as contrast and frequency of a moving stimulus. For example, with increasing contrast and high frequency, latency decreases. Moreover, temperature changes and the age of the fly affects the latency [59]. [60] reports that motion sensitive neuron H1 (compound eye neuron) transmits signals in 20-30ms. [58] measures 6ms for ocellar latency, which indicates a significant reduction when compared to compound eyes. For high frequency disturbances, low-latency ocellar neurons will be needed.

Fusion Approaches

In motion detection and control systems, especially in flight control and inertial navigation, different kinds of sensors are used on one platform. When measuring a particular variable, a single type of sensor may not be able to meet all the required performance specifications. For example, both accelerometer and gyroscope data can be used to compute angles. Since accelerometer gives acceleration, angles can be reconstructed from accelerometer output by two-fold integration. Similarly, gyroscope gives velocity information and one integration would be enough. Accelerometer is known to be good for 'long-term', meaning that it does not drift. Gyroscope is good for 'short-term', is known to have poor drift characteristics, however it is able to give fast response. An ideal combination would be a fast transient response with no drift, by combining good qualities from two measurements. Theoretically, if a time varying signal is applied to both a low-pass and high-pass filter with unity gain, the sum of the filtered signals should be identical to the input signal. (See Figure 45). Assume that x and y are noisy measurements of some signal z, x employing low-frequency noise and y employing high-frequency noise. z' is the estimate of the signal z produced by the complementary filter.

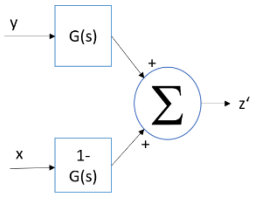

Figure 45: Illustration of complementary filter.

Practically, complementary and Kalman filters provide the fusion of two signals. Kalman filter, working in time domain, needs statistical description of the noise corrupting the signals. This noise is assumed to be Gaussian white noise. Complementary filters approach the problem from the frequency domain, and they are generally used for the fusion systems that do not deal with noise. For digital implementation, the complementary filter has considerable advantage over Kalman filter, because Kalman gains are not computed for each state. Therefore, after determining the filter coefficients for complementary filter, the update rate of complementary filter can be higher than Kalman filter for each loop. This is an important consideration for the applications in which high-rate loop closure is necessary.

Previous Sensor Fusion Implementations

Sensor fusion is governed by complementary and Kalman filtering in the literature, generally for virtual reality applications in computer vision and attitude control. Vision-based information helps avoiding the errors resulting from integrating the inertial sensors over time. [61] fuses two accelerometers and three gyroscopes for an indoor mobile robot to obtain attitude information using extended Kalman filter. [62] fuses gyroscopes and inclinometer for head-tracking using Kalman filter. [63] integrates high-frequency stable gyroscope and low-frequency stable vision-based tracking using Kalman filter for an augmented reality. [64] uses extended Kalman filter that takes information from camera images, inertial measurement unit and magnetometers to estimate the pose of the vehicle. [65] fuses accelerometer, gyroscope and vision sensors to obtain position, velocity and attitude information for UAV, using a nonlinear complementary filter framework. [66] uses extended Kalman filter to fuse vision-based output for slow movements and inertial sensor output for fast movements for virtual

reality applications. [67] uses Kalman filter to fuse data from three accelerometers and three gyroscopes with a position sensor, for UAV navigation. Position sensor input is either from GPS, when GPS is available, or from vision system (feature tracking) when GPS is not available. [68] fuses GPS data, inertial sensor data and camera image data for global pose information for augmented reality. Inertial and GPS data is fused using Kalman filter. [69] uses extended Kalman filter to fuse air pressure sensor and vision framework (computationally expensive) with inertial sensor data to handle the fast movements and disturbances of the MAV. [70] proposes a complementary filter to fuse magnetometer, accelerometer and gyroscope for attitude estimation. In this chapter, the time domain signal of both ocellar and optic flow outputs are combined to extend the optic flow frequency response.

Ocellar Sensor-Optic Flow Fusion Approach

Previous results show that optic flow shows roll-off at high frequency motion. On the other hand, ocellar sensor shows a relatively flat response at high frequencies. This experiment uses a camera capable of 87 fps in theory, and a high-speed Ubuntu laptop. Even with this configuration, the real frame rate obtained from the camera becomes 60fps, because of data transfer limitations of USB busses. The frame rates higher than 60fps result in dropped frames and corrupts the optic flow output. Commercially available single-board computers (e.g. [71]) allow for lower frame rates. Practically, Raspberry Pi 2 is limited to 15-20 fps for the same Lucas- Kanade algorithm used in this experiment. A more expensive model, Odroid XU4 [72], is capable of 60 fps, however its cost doubles Raspberry Pi ($75 vs. $35). A relatively cheap single-board computer will have a limited optic flow computation bandwidth. On the other hand, ocellar sensor offers a fast, cheap and low-power alternative to optic flow computation. It has a relatively flat magnitude and phase response, it is an attractive alternative for rotational motion. However, its performance is highly dependent on the luminance. It assumes a constant luminance gradient from sky to ground. Optic flow computation does not have such an assumption, it only needs a texture around it. Moreover, this setup uses a 180° field-of-view lens to obtain wide-field motion. To have more field-of-view, the number of cameras may be increased,

however this will bring a necessity for simultaneous triggering of the two cameras. When this setup is used with two cameras, the triggering reduces the camera frame rates down to 20 fps. This reduction is expected to be more using a cheaper configuration. Lower frame rate will introduce a lower optic flow bandwidth, making the optic flow sensing incapable of performing at high frequencies. To compensate for the high-frequency roll-off of optic flow, ocellar sensor data is fused with optic flow. The optic flow data is low-pass filtered with a 4th order Butterworth filter. The inverse of this filter, a 4th order Butterworth high-pass filter with the same cutoff frequency is used to high-pass filter the ocelli data. The reason to use for 4th order Butterworth filter, instead of single-pole high and low-pass filters is that it resulted in a better coherence. Single-pole filter combinations decreased the coherence values at high frequencies. The fusion operation increased the bandwidth and decreased the phase delay of optic flow.

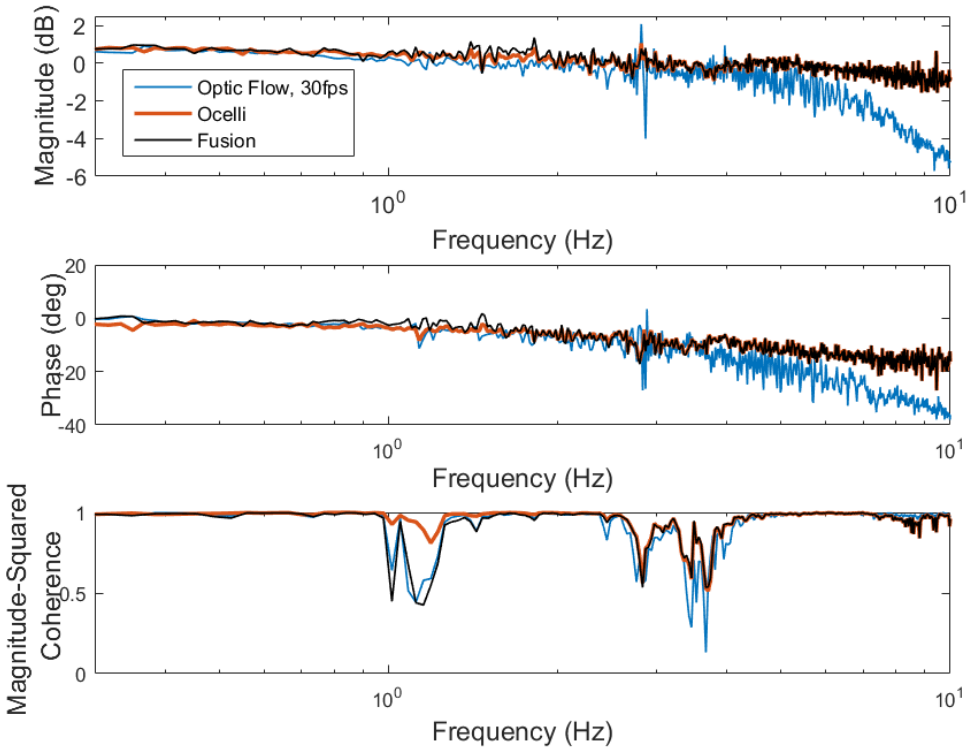

Figure 46: Frequency response ocelli , optic flow, and their complementary fusion: 4th order Butterworth filter was used to high-pass ocelli and low-pass optic flow. The normalized cutoff frequency had to be kept very small to

make use of ocelli's relatively plat magnitude and less-delayed phase. Fused response shows coherence is better than optic flow's.

An even more direct way is taking the weighted average of optic flow and ocelli. While this approach will not give a fully low-pass filtered optic flow and high-pass filtered ocelli, if the ocelli weight is kept high, the result will be very similar to optic flow. Figure 47 shows another fusion that implements:

$$a * ocelli + (1 - a) * optic\ flow \quad (48)$$

Where a=0.9. Magnitude, phase and coherence plots result in-between ocelli and optic flow, very close to ocelli.

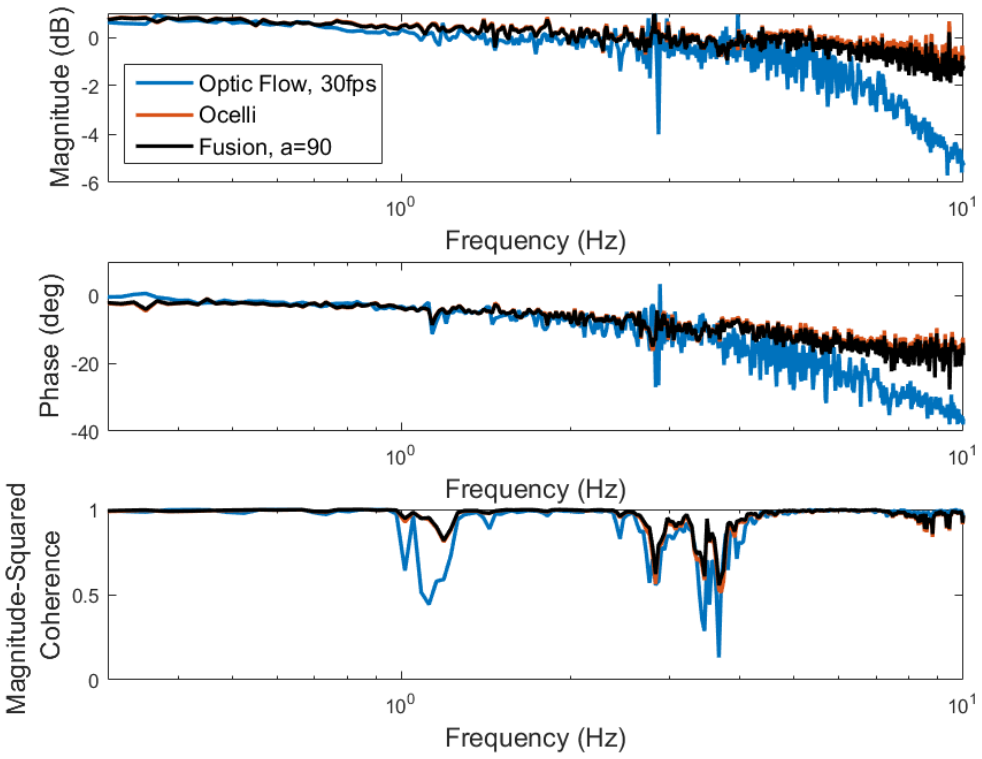

Figure 47: Frequency response ocelli , optic flow, and their weighted-average fusion: Ocelli and optic flow time-domain signals are combined to obtain a result close to ocelli.

However, complementing both ocelli and optic flow readings gives a result close to ocelli. It assumes that the ambient luminance distribution is as calibrated in this experiment. We know that the ocelli magnitude increases with increasing luminance. This peak-to-peak amplitude is a linear function of input light source power, as seen in Chapter 3. Additionally, ocellar sensor has to be in a 'valid range'. All in all, optic flow is immune to luminance intensity. It gives a flat magnitude response at low frequencies. Ocelli, however, is vulnerable to luminance intensity and it does not show a roll-off in magnitude as optic flow shows. It would be ideal to combine the good properties of both measurements real-time. Ocelli magnitude plot with respect to increasing luminance intensity should result in a plot like Figure 48. Optic flow magnitude plot shows a low-pass characteristics.

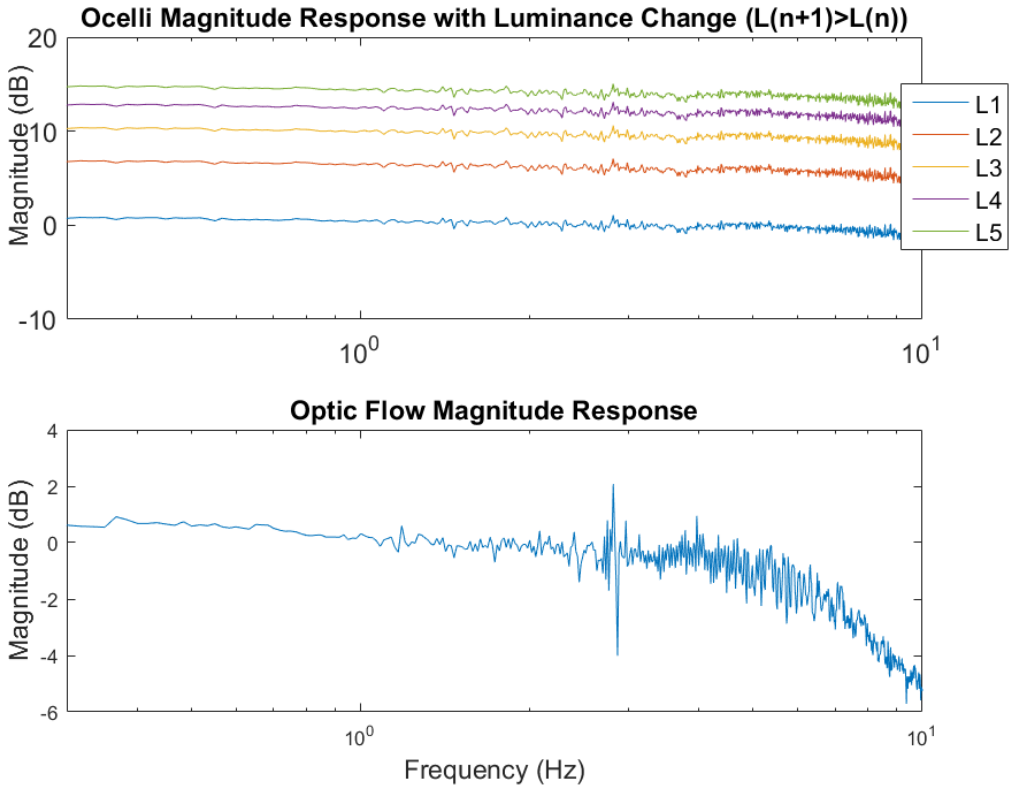

Figure 48: Magnitude response of ocelli with different luminance values and optic flow at 30 fps: Increasing luminance implies higher magnitude for ocelli ($L_1 < L_2 < L_3 < L_4 < L_5$). Ambient luminance change brings adaptive

gain necessity. Upper figure is the magnitude-scaled versions of ocelli response, not derived from real luminance values.

A mechanism that allows for switching from one mode to another is desired to decide which sensor to use. This switching mechanism may be gyroscope. The gain adjustment may be done with a feedback from ocelli output that is continuously compared with gyroscope/optic flow output. If a valid region for ocelli is found, ocelli is preferred over optic flow due to its high-speed. A hypothetical iterative approach is shown in Figure 49. First, ocelli gain is adjusted with the use of a lookup table and the error between ocelli and gyro is computed. If this error is below a threshold, the gain adjustment is satisfied. After this, the validity of ocelli output is confirmed by computing the error between gyro and optic flow. If these comparisons allow, ocelli is preferred to be used for closed-loop rate stabilization. If not, either gyro or optic flow is used. Ocelli gain can be adjusted with digital potentiometers and an operational amplifier. The digital potentiometers are controlled from microcontroller. For a gain<1, a voltage divider reduces the ocelli output. For a gain>1, a non-inverting amplifier increases the ocelli output. This output is continuously fed back to the microcontroller to compare the gyroscope and ocelli error, to find a new gain value from the lookup table and adjusting the potentiometers accordingly. Figure 50 shows the possible circuit configuration and connections with microcontroller.

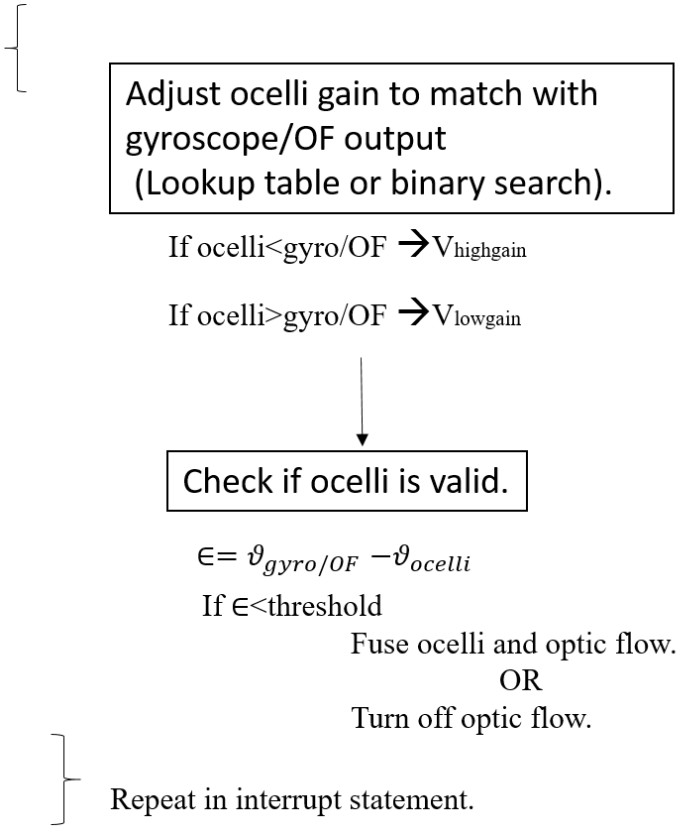

Figure 49: Sensor decision approach: Adjust ocelli gain by continuously computing error between gyro/OF and ocelli, check if ocelli is valid to use by comparing gyro/OF, use ocelli of comparisons allow.

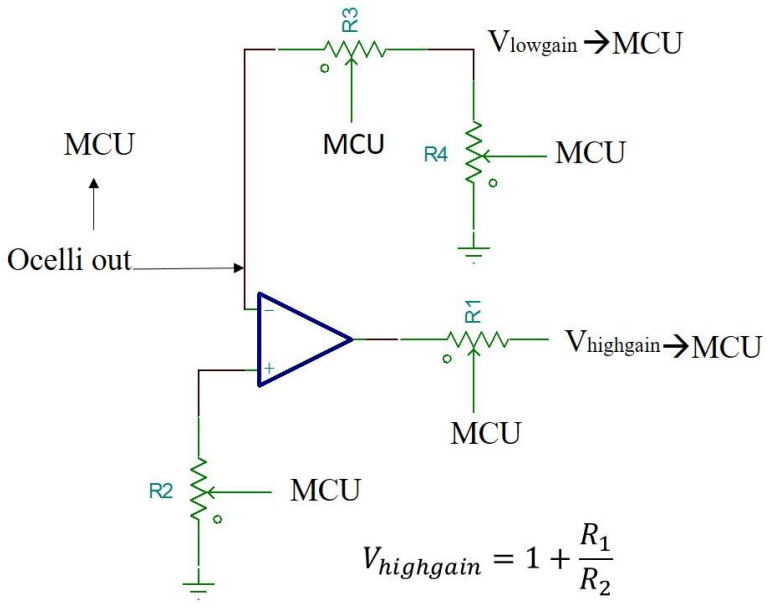

Figure 50: Ocelli gain adjustment approach: Gains>1 are tuned by non-inverting op-amp. Gains<1 are tuned by voltage divider. The tuned outputs are compared with lookup table and microcontrollers iteratively tune the digital potentiometers until error threshold is low enough.

Chapter 5: Conclusion and Future Work

Conclusion

Frequency-domain characterization of optic flow and ocellar sensors are presented. The advantages and disadvantages for both sensing mechanisms are discussed. In summary:

1. Ocellar sensor shows a relatively flat magnitude response and less phase delay than optic flow.
2. Ocellar sensor is attractive for high-rate loop closure since it is cheaper and faster from high-quality cameras.

3. The displacement dynamic range of the ocellar sensor is observed to be 1 radian with this setup, due to the small size of the light source. Using a bigger light source, higher displacements may be achieved.
4. The frequency dynamic range of ocellar sensor is observed to be up to 10 Hz with motion, and up to low-frequency cutoff without motion. 10 Hz is a limitation from mechanical test setup, higher motion frequencies are expected due to the circuit simulation and LED experiment results. For outdoor experiments, the low-frequency cutoff of the band-pass circuit can be eliminated, since there is no flickering issue outdoors.
5. Ocellar sensor magnitude shows a linear relationship with luminance intensity. Since it is highly luminance-dependent, an adaptive gain calibration is necessary for usage with different luminance levels.
6. Ocellar sensor shows monotonic increase with increasing gyro values.
7. Optic flow magnitude rolls off at high frequencies. Specifically, 60 fps can keep up with ocelli response. 30 and 20 fps show roll-off at 7 Hz. Less frame rate shows steeper roll-off. Phase delay increases with increasing frequency. All frame rates tested show the same phase delay across all frequencies.
8. Optic flow algorithm parameters (feature points, window size) affect the coherence. No significant change in magnitude and phase plots is observed, except for erroneous magnitudes for extremely small window sizes or feature points.

Future Work

Several potential directions may be taken to extend the work of this thesis. Taking the characterization results, performance parameters and hypothetical sensor fusion suggestions into account, a closed-loop optic flow and ocellar-based fusion may be implemented to perform real-time stabilization and disturbance rejection. Multiple ocellar sensors with lenses may be placed in an array-like fashion on a

flying vehicle to extend the current field-of-view of the ocellar sensor. The outputs of ocellar sensor may be matched with pre-defined patterns to inform where exactly the disturbance occurs.

The combination of optic flow computations and ocellar sensor gives both slow and fast alternatives for horizon detection and angular-rate sensing.

The coherence in ocellar sensor and optic flow frequency response plots show dips at specific frequencies. The reason for these dips could not be identified during the experiments. If these dips were caused form the motor mechanical noise, both the gyroscope and the ocellar sensor should be able to pick the mechanical noise up, resulting in the same motion for both of them. Also, the motor resonance and gyroscope resonance possibilities have been eliminated after confirming the time-domain signals with the ground truth. It is presumed that the ocellar sensor may be slightly modulating the input sine wave at these frequencies. The experiments can be repeated by using another ocellar sensor board and/or another motor.

To compensate for optic flow's slow rate, another direction might be converting the optic flow-ocelli system to a fully analog scheme. Combining both sensors in analog domain might give the complementary approach in a compact, fast and lightweight way. While digital optic flow computation has the freedom of easy adaptation and reconfiguration with different, sophisticated, and robust algorithms; sub-threshold analog VLSI optic flow designs are much smaller, lightweight, low-power and faster. One may argue that the one-board computers are already lightweight. However, decrease in size and weight are extremely important factors for micro aerial vehicle design. VLSI allows the photodiodes and computation circuitry to be fabricated on a piece of silicon, therefore it is very suitable for vision-based sensing.

Appendix B includes spectral sensitivities of different insect ocelli. Insect ocelli are highly responsive to ultraviolet wavelengths. A completely different direction might be taking the ocellar sensor outside, using the sky-ground discrimination in ultraviolet wavelengths. The wide-band photodiodes in current circuit can be replaced with ultraviolet photodiodes. A detail to consider is the ultraviolet intensity difference in sky and ground in different times of the day and different weather conditions. On a sunny

day, the results show that sky is brighter than ground in ultraviolet. On a cloudy day, it can be the opposite. While the constant and negative luminance gradient may not be satisfied for all cases, specific weather conditions (e.g. sunny day, no clouds) can allow for outdoor use. We have built the ultraviolet version of the ocellar sensor and tested outside. A main problem is the uneven ultraviolet intensity coming to both ultraviolet photodiodes. On cloudy days, there is nearly no ultraviolet difference between sky and the ground, it is thought that the clouds are blocking the ultraviolet portion in the sunlight. On sunny days, one photodiode should not see the high intensity created by the sun, and should only have the portion coming from the sky. The instantaneous displacement of the clouds and the wind are also factors that create the uneven ultraviolet intensity on both photodiodes. While these cases make it hard to test outside, we have seen with some datasets that agrees with gyroscope output.

Appendix A: Code Information

C++ Codes

Communication with Camera

Optic Flow Computation

Communication with Motor

Communication with Microcontroller

Matlab Codes

Chirp Trajectory

Sine Trajectory

Bag File Extraction & Data Parsing

Arduino Code

Communication with MCP3008 ADC

Communication with Gyro

Appendix B: Sky-Ground Discrimination in Ultraviolet Wavelengths

Introduction

We attempt to explore the usability of ultraviolet light for vision sensing. In other words, 'Does ultraviolet vision provide useful information about the separation of sky and ground?'

First, insect responsiveness to ultraviolet and near-ultraviolet light is discussed. Second, ocelli spectral responses from several species are listed from the literature. Third, photos taken with ultraviolet filter are analyzed. Lastly, experimental data measured with an analog ultraviolet sensor in different weather conditions is analyzed.

Biological Background

The light emitted from sources and reflected from objects contain different wavelength information. A very general classification can be made based on the fact that light coming from sources (e.g. sun, moon or sky) is characterized by its high content of UV and near-UV wavelengths. However, light coming from objects or soil lacks UV wavelengths. [73] suggests that this distinction between direct and reflected light might be a cue, which allows an animal to navigate itself in its natural habitat, such as differentiating between open spaces, shadowed areas or hiding places.

Unlike humans, insects are able to make use of UV light. They are sensitive to a broad range of wavelengths from UV to red. Color sensitivity in UV spectrum is believed to play an important role in insect navigation and mate selection in both flying and terrestrial invertebrate animals. The response to UV leads to different reactions. When insects are exposed to light, they may show positive or negative phototaxis (they may go towards or fly away from the illuminator). Interestingly, even the lethal effects of UV and near-UV wavelengths are being used against the insects for pest management [74, 75].

[76] experiments that flies can discriminate relative motion of an object and its background, even when the object and background texture are identical, provided that there is relative motion between the object and ground. A fly follows a black object (on a white background), while the object is moving with a constant angular velocity. The tracking angle is related to the angular velocity of the object and the contrast between object and the background. Especially the contrast difference is important for the tracking angle. [77] studies the computation of this effect experimentally, concluding that the outputs of neighboring movement detectors interact in a multiplication-like fashion. [78] studies the neuronal circuitry used in this phenomenon with electrophysiological studies and models a circuitry for this purpose. [79] further investigates this effect with electrophysiological and behavioral experiments, stating that only one cell type (Horizontal Cells) cannot be used for object-ground discrimination on their own. Additional output cells of optic lobes with different functional properties are required to accomplish this task. [25] conducts behavioral experiments on locusts with a simulated horizon. Horizon motion results in motion in animal's head during flight. When the ocelli are surgically ablated, the compound eyes are able to mediate visual head stabilization and flight steering behavior over a wide range of conditions. However, the operation introduces latency. It also suggests that ocelli increase the amplitudes of visual response. Another point to note is that, when there are sharp borders, only compound eyes are able to provide visual responses. However, when the border is not sharp enough, this is not the case and ocelli are needed. It is suggested that ocellus may be averaging illumination intensity over its field of view. The increase and decrease in overall illumination intensity results in a visual response.

There is no known insect species that have only ocelli. Ocelli are not known to exist independently from compound eyes. Moreover, from the information above, we know that some flies are able to continue their head and steering movements without ocelli. This information might suggest that ocelli are only helpers to compound eyes for better flight abilities. However, the functional dominance of ocelli over compound eye may vary among species. For example, dragonfly, employing both compound eyes and ocelli, is known to have exceptional aerodynamic maneuvers and ability to

stabilize its flight for sudden motions. [23] suggests that, for dragonfly ocelli, compound eyes and ocelli help equivalently to the flight behavior. The ocelli uses second order neurons, whereas compound eyes use higher order neurons, introducing a time delay in information processing. Ocelli, by employing less neuron hierarchy, eliminates this time delay effect and allows for quick information processing for sudden disturbances, which is crucial for dragonfly flight.

Previous Sky-Ground Separation Implementations

[80], inspired by the high responsiveness of desert ant ocelli to ultraviolet and green wavelengths, collects outdoors images in visible, ultraviolet and green wavelengths with a standard camera. It is suggested that the segmentation of the sky using only UV is significantly more accurate and consistent than visible wavelengths over a wide range of locations, times and weather conditions. Performance is the worst using visible light, as sky and ground are not easily separable when clouds are present. In contrast, sky and ground naturally separate along the UV dimension, giving robust segmentation in UV and UV-Green images. [81] shows a statistical comparison in five spectral channels: Ultraviolet, red, blue, green, near-infrared. It is suggested that contrasts with large differences in the wavelength of two channels (e.g. UV+IR, blue+IR, UV+red) yield the best separation. Among single channels, the best separation is obtained in ultraviolet light. [82] presents a panoramic vision-based attitude determination a CCD camera, ultraviolet filter and panoramic mirror-lens. However, the comparison between UV and any other wavelength was not reported.

Besides from using ultraviolet, [83] suggests a polarization-based segmentation approach for attitude estimation. [84] suggests combining red, green and blue (RGB) components of each pixel value into a single pixel with the formula $3B^2/(R+G+B)$, using horizon video. This formula is the product of blue component of the image B/(R+G+B) with the mean overall RGB intensity value (R+G+B)/3. [85] validates this method with a helicopter platform, using a catadioptric camera.

[86] suggests converting the RGB values of images into a single color component with a specific equation. They determine a threshold by applying a score to each color value, based on histogram data, then estimate altitude. Also, [87] proposes segmentation using thermal infrared band with thermopile sensors.

Ocelli Spectral Sensitivities

Studying the insect color vision is rewarding due to the highly diverse color receptors across species, offering great evolutionary adaptation. [88] suggests that insects may perceive landmarks as a silhouette, against a skyline as the background.

Table B1 summarizes the peak spectral responsiveness of several insect ocelli. We acknowledge Air Force Office of Scientific Research to provide us with this table, hence most of the references are very old and hard to find online, or are not open to school network. For these experiments held from 1950s to 2000s, electro-retinography (ERG) was used to measure the electrical responses of ocelli photoreceptors. Among 22 species, 16 show peak responsiveness at ultraviolet and near-ultraviolet wavelengths (300-400 nm). 1 show peak at blue (~475nm) and 1 show peak at orange (~600nm). 18 show peak responsiveness at green wavelengths (~510nm). From the very general assumption that light coming from the sources contain more UV content, it seems reasonable to ask whether the insect is using this ultraviolet content to separate sky from ground or landmarks.

Table B1: Spectral sensitivities of different insect ocelli

Class	Order	Family	Binomial	Common Name	UV	NEAR - UV	BLUE	GREEN	YELLOW	ORANGE	RED	SOURCE
Branchiopoda	Anostraca	Artemiidae	Artemia Salina	Brine Shrimp		410						Hertel, 1972
Hydrozoa	Anthomedusae	Polyorchidae	Polyorchis penicillatus					530				Weber, 1982a
Hydrozoa	Anthoathecata	Corynidae	Sarsia tubulosa	Sarsia-Medusa				540				Weber, 1982b
Insecta	Blattodea	Blattidae	Periplaneta americana	American Cockroach				500				Goldsmith & Ruck, 1958
Insecta	Coleoptera	Lamprydae	Luciola cruciata	Japanese Firefly				530				Hariyama, 2000
Insecta	Coleoptera	Lamprydae	Luciola leteralis	Japanese Firefly				530				Hariyama, 2000
Insecta	Diptera	Culicidae	Aedes Aegypti	Yellow Fever Mosquito	370			520				Seldin et al, 1972
Insecta	Diptera	Drosophilidae	Drosophila melanogaster	House Fly	350-370	445						Hu et al, 1978
Insecta	Hymenoptera	Apidae	Bombus hortorum	Bumble Bee	353			519				Meyer-Rochow, 1980
Insecta	Hymenoptera	Apidae	Apis mellifera	Western Honey Bee	335-340		490					Goldsmith & Ruck, 1958
Insecta	Lepidoptera	Noctuidae	Trichoplusia ni	Cabbage Looper Moth	360			530				Eaton, 1976
Insecta	Lepidoptera	Pieridae	Pieris brassicae	Cabbage Butterfly	370	460				600		Land & Nilsson pg. 29
Insecta	Lepidoptera	Pieridae	Pieris rapae	Small White Butterfly	360	425/453						Warrant & Nilsson pp.30
Insecta	Lepidoptera	Sphingidae	Deilephila elpenor	Elephant Hawk Moth	345	440		520				Hardie & Stavenga
Insecta	Lepidoptera	Sphingidae	Manduca sexta	Goliath Worm	360			520				Eaton & Pappas, 1978
Insecta	Mantodea	Mantidae	Tenodera sinensis	Praying Mantis	370			510-520				Sontag, 1971
Insecta	Odonata	Anisoptera	Anax junius	Green Darner	360	440		500				Chappell & DeVoe, 1975
Insecta	Odonata	Anisoptera	Aeshna tuberculifera	Black Tip Darner	360			500				Chappell & DeVoe, 1975

Insecta	Odonata	Anisoptera	Libellula pulchella	Twelve-Spotted Skimmer	360			500				Chappell & DeVoe, 1975
Insecta	Odonata	Corduliidae	Hemicordulia tau	Emerald Dragonfly	360	440		510				Mizunami, 1994
Insecta	Orthoptera	Acrididae	Locusta migratoria	Migratory Locust	370			500				Wilson, 1978
Insecta	Orthoptera	Gryllidae	Gryllus firmus	Field Cricket				520				Lall & Trouth, 1989
Tubellaria	Tricladidae	Planariidae	Planarian (family)	Flatworm				508				Brown et al, 1968

Ultraviolet Photography Analysis

We tried taking ultraviolet photos with black light bulb pieces and HOYA U340 [89] UV-passing and visible-absorbing filter using a Canon professional camera. However, we could not succeed due to the internal UV and IR blocking filters of the camera. HOYA U340 lens has a little transmittance in near-IR region, the photos obtained had only red component in them with black background. We greatly acknowledge Dr. Enrico Savazzi from Uppsala University for providing us the UV photos. They have been recorded with a variety of filters with transmission windows approximately in the 320-390nm range and 300-380nm range, mostly with the Baader U-Filter, which has its peak at 360-370 nm. These images are false colored images. The blue and violet correspond to long UV wavelengths near the visible spectrum (~390-400nm). Red is around 380nm, yellow is around 365nm, green is around 320-340nm.

Figure B51: Ultraviolet photo 1

Figure B52

From the landscape in Figures B1 and B2, it can be said that sky is homogeneously separated from the ground. The difference between the vegetation (trees in black in Figure B1, stones in Figure B2) and sky is noteworthy, however, the textures on the ground can lead to false labeling (e.g. sky-like gas station signs in Figure B1 and bright signs on textures in Figure B2).

Figure B3 shows a sky-ground separation without texture on the ground, which suggests that there is a brightness difference between ground and sky UV components.

Figure B5 introduces a cloudy sky as background. In compared to its possible visible equivalent, clouds seem to introduce a more homogeneous sky brightness. Although there is significant brightness difference between the chateau and the sky, the light texture in the garden has a comparable brightness value with the sky, which again, may lead to false labeling.

Figure B53

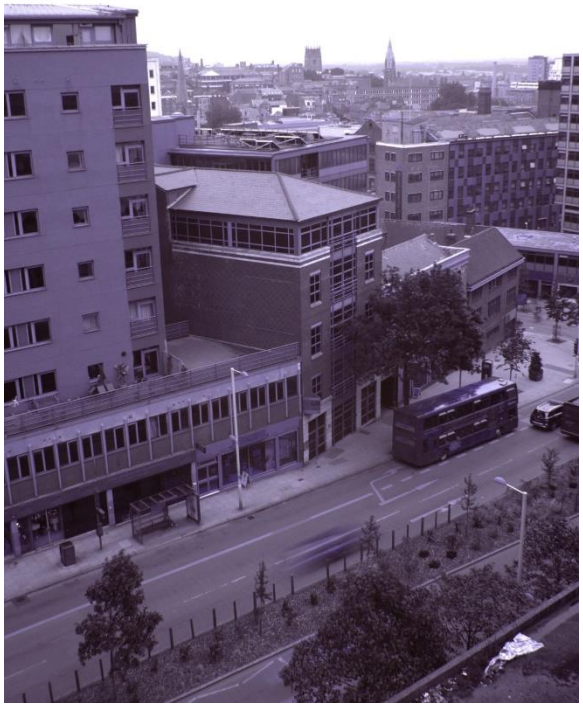

Figure B54

Figure B5

Figure B6

Figure B6 includes cloudy sky, water scene, vegetation and asphalt. Although there is brightness difference between sky and ground components, the reflection from the water creates a comparable brightness with the sky, suggesting a possible false sky labeling.

Figure B7

Figure B4 has a sky with saturated brightness. The sky is homogeneously saturated, resulting in a single brightness level. The buildings introduce a notably homogeneous and different brightness level in compared to the sky. The bright sides of the buildings, probably resulting from the UV reflectance from the sun, seem to be separable from the sky. However, a few buildings show comparable brightness levels. Figure B7 shows an unsaturated cloudy sky with vegetation and white tombstones as surroundings. The vegetation employs homogeneous brightness level, which again simplifies its identification. Although not saturated as in Figure B4, the cloudy sky shows a more homogeneous color distribution in compared to

its visible equivalent. However, the tombstones on the ground also make only UV-based sky-ground separation questionable.

From these photos, without any reflective/bright textures in the ground, it may be suggested that UV-based sensing may provide a better sky-ground segmentation, with constrained environments that contain only vegetation and sky (e.g. forests).

Ultraviolet Sensor Response Analysis

We present experimental data taken from an analog-based UV intensity sensor in different environmental conditions, with the aim to extend the usage of the current analog ocellar sensor to outdoors.

Figure B8 shows the test setup used to measure the ultraviolet intensity. An analog-based UV intensity sensor [90] and an amplifier circuit are used to take intensity measurements along an arc, in different weather conditions. The gain of the amplifier is varied due to different brightness levels in different days. LM324N general purpose operational amplifier was used with discrete resistors, soldered on a printed circuit board. The spectral responsivity of the UV sensor varies between 240-380 nm, showing peak responsivity at 360 nm. The field of view of the sensor is restricted by a thin tube. For every 10°, analog sensor measurements are sent to Arduino Uno's 10-bit 10kHz analog-to-digital converter (ADC) and data is recorded from the usb-serial port, for three times. For the same angle, around 100 data points are taken and the average is calculated. The measurement is limited by Arduino UNO's ADC, which has a resolution of 4.9 mV.

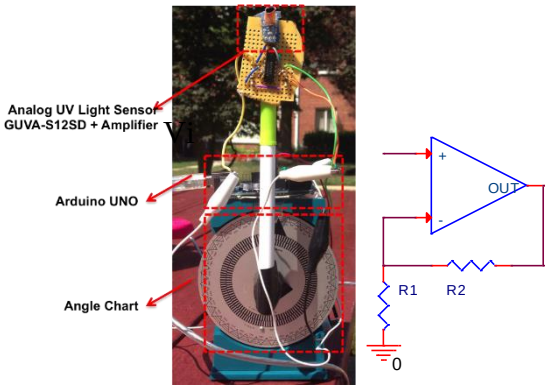

Figure B8: UV intensity test setup and the non-inverting amplifier configuration

Figure B9 shows UV sensor output versus angle on a cloudy day. Test scene and the arc are seen in the photo above the graph. The sensor output is recorded between -140° to +140°. Sun is coming from the left of the photo. The borders between the vegetation and the sky are -95° and +90° on the left and right, respectively. Sensor starts around 1500mV while seeing the vegetation on the left. The output starts to increase when the sensor view leaves the vegetation. The non-homogeneous distribution of the clouds and the sunlight causes two peaks, both of which are significantly separable from the vegetation effect. Because of the decrease in brightness and the different height of the trees, the output decreases down to 600 mV. A third peak is introduced at 900 mV, which may be from the reflectance due to the sunlight coming from the left onto the trees.

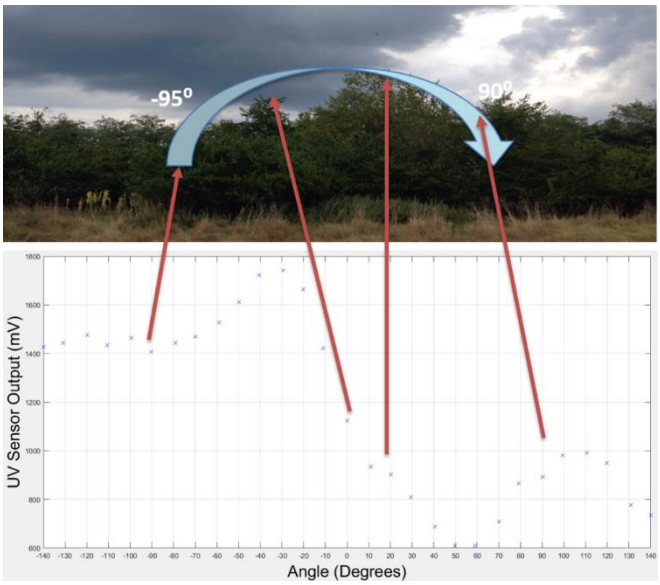

Figure B9: Ultraviolet measurement on a cloudy day

Figure B10 shows the measurement on a sunny day at 12 PM. The sun is at the right of the photo. The sky shows an opposite effect in compared to Figure B9 results. UV light coming from the sky is less than the one reflected from the vegetation. The arc leaves the vegetation at -60°, from which the UV output starts to decrease. It comes as low as 800-1000 mV at +15°, then starts to increase. The arc leaves the sky at around +65°, after which the output seems to be stabilized around 1500 mV. The output difference between the left and the right side of the vegetation may be due to the reflectance, hence the location of the sun. The sun, coming from the right back, illuminates the left side more than the right side.

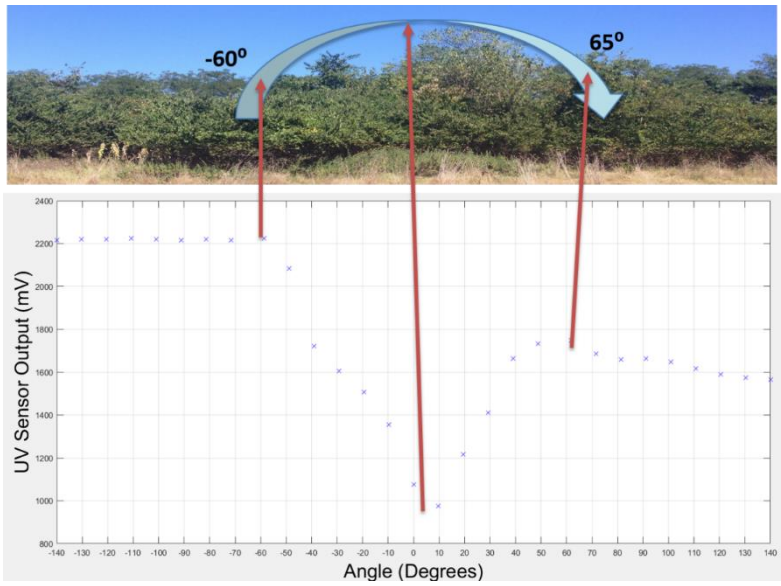

Figure B10: Ultraviolet measurement on a sunny day

Figure B11 shows the measurement on a sunny day at 1 PM, with a different scene. The sun is just above the photo. Different reflections from the lake and the vegetation complicates the measurement results, however, UV coming from the sky is again less than the one reflected from the surroundings. The arc enters to the sky at -80°and leaves the sky at +80°.

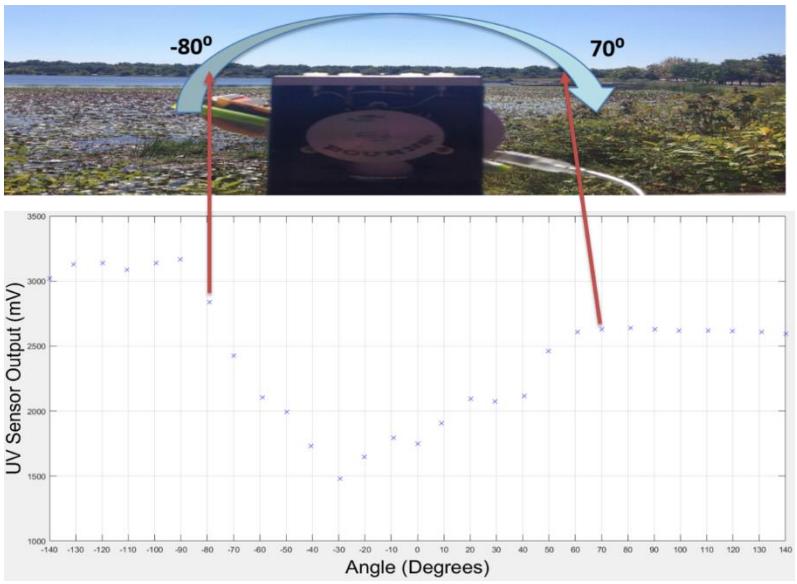

Figure B11: Ultraviolet measurement on a sunny day, different scene

Figure B12 shows the measurement in a sunny weather at 6 PM. The sun comes from the left back of the photo. The arc leaves the vegetation at -75°, from which the output starts to decrease. It becomes as low as 300 mV at -10°, then starts to increase. It leaves the sky at +50° and meets the vegetation. The output seems to be stabilized at around 600 mV.

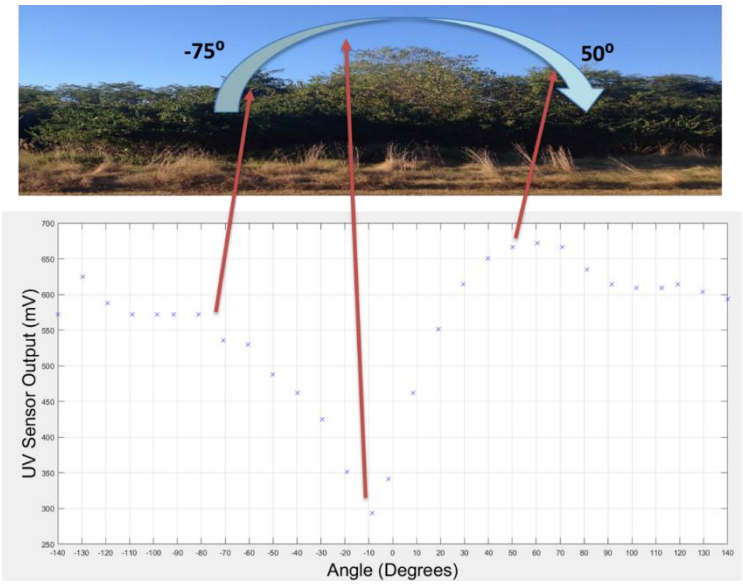

Figure B12: Ultraviolet measurement on a sunny day, 6PM

Discussion

As reported in the above measurements, our argument 'The sky is brighter than ground in ultraviolet' is not a generalizable argument. Sky-ground separation cannot solely rely on ultraviolet intensities alone. Different weather conditions (e.g. cloudy vs. sunny) give different relative ultraviolet intensities. The brightest levels are at least two times brighter than the darkest levels. For a single dataset, e.g. cloudy weather at 12 pm, a threshold could be defined that would assign a separation line between sky and ground. This threshold value would not be reliable, since there is different ultraviolet intensities in different times of the day. From the data, the reason of this change seems to be related to several parameters: Location of the sun, reflection from the ground and the vegetation, clouds hiding ultraviolet coming from the sun.

If ultraviolet is used with a "local" threshold (e.g. a threshold value range for only cloudy weather), this mechanism will bring a necessity for adjustable threshold. An optimal threshold, lying between the brightest and the darkest points in the sky, varies over a range of almost four magnitudes. A possible

reference point may come from measuring the intensity in zenith, however, it is questionable if such a reference would work under inhomogeneous sky.

Another point worth mentioning is that, water points, seen in Figure B6, will not be distinguishable with a threshold method. If the navigation is around a large lake, the lake may bring a false horizon.

Bibliography

[1] Barth, F. G., Humphrey, J., and Srinivasan, M., *Frontiers in sensing: from biology to engineering*. Springer Science & Business Media, 2012.
[2] Available: https://en.wikipedia.org/wiki/Simple_eye_in_invertebrates (Last reached 05.06.2016)
[3] Available: https://en.wikipedia.org/wiki/Arthropod_eye (Last reached 05.06.2016)
[4] Available: http://cronodon.com/images/Ommatidium_3.jpg (Last reached 05.06.2016)
[5] Mazokhin, G.A., *Insect Vision*. New York: Plenum Press, 1969. Hardcover
[6] Horridge, G.A., *Compound Eye and Vision of Insects*, New York: Oxford University Press, 1975. Hardcover
[7] Joesch, M., et al. "ON and OFF pathways in Drosophila motion vision." *Nature* 468.7321 (2010): 300-304.
[8] Borst, A. "Fly visual course control: behaviour, algorithms and circuits." *Nature Reviews Neuroscience* 15.9 (2014): 590-599.
[9] Wallace, G. K. "Visual scanning in the desert locust Schistocerca gregaria Forskal." *J. exp. Biol* 36 (1959): 512-525.
[10] Silies, M., Gohl, D. and Clandinin, T.R. "Motion-detecting circuits in flies: coming into view." *Annual review of neuroscience* 37 (2014): 307-327.
[11] Kral, K., and Michael P. "Motion parallax as a source of distance information in locusts and mantids." *Journal of insect behavior* 10.1 (1997): 145-163.
[12] Sobel, E. C. "The locust's use of motion parallax to measure distance."*Journal of Comparative Physiology A: Neuroethology, Sensory, Neural, and Behavioral Physiology* 167.5 (1990): 579-588.
[13] Schnell, B., et al. "Processing of horizontal optic flow in three visual interneurons of the Drosophila brain." *Journal of neurophysiology* 103.3 (2010): 1646-1657.
[14] Haag, Juergen, Denk, and Borst. "Fly motion vision is based on Reichardt detectors regardless of the signal-to-noise ratio." *Proceedings of the National Academy of Sciences of the United States of America* 101.46 (2004): 16333-16338.
[15] Frye, M. "Elementary motion detectors." *Current Biology* 25.6 (2015): R215-R217.
[16] Available: https://en.wikipedia.org/wiki/Insect_morphology (Last reached 05.06.2016)
[17] Stange, G., et al. "Anisotropic imaging in the dragonfly median ocellus: a matched filter for horizon detection." *Journal of Comparative Physiology A*188.6 (2002): 455-467.
[18] Wilson, M. "The functional organisation of locust ocelli." *Journal of comparative physiology* 124.4 (1978): 297-316.
[19] Goodman, L. J. "Organisation and physiology of the insect dorsal ocellar system." *Handbook of sensory physiology* (1981).
[20] Heisenberg, M., and Reinhard W. *Vision in Drosophila: genetics of microbehavior*. Vol. 12. Springer-Verlag, 2013. Hardcover
[21] Kastberger, Gerald, and Klaus Schumann. "Ocellar occlusion effect on the flight behavior of homing honeybees." *Journal of insect physiology* 39.7 (1993): 589-600.
[22] Schricker, Burkhard. "Die Orientierung der Honigbiene in der Dämmerung."*Zeitschrift für vergleichende Physiologie* 49.5 (1965): 420-458. (Summary in English available at Springer)
[23] Stange, G. and Howard, J. "An ocellar dorsal light response in a dragonfly." *J. exp. Biol* 83 (1979): 351-355.
[24] Stange, G. "The ocellar component of flight equilibrium control in dragonflies." *Journal of comparative physiology* 141.3 (1981): 335-347.
[25] Taylor, C. P., "Contribution of compound eyes and ocelli to steering of locusts in flight: I. Behavioural analysis." *Journal of Experimental Biology* 93.1 (1981): 1-18.
[26] Schuppe, H., and Hengstenberg, R. "Optical properties of the ocelli of Calliphora erythrocephala and their role in the dorsal light response." *Journal of Comparative Physiology A* 173.2 (1993): 143-149.
[27] Rence, B. G., et al. "The role of ocelli in circadian singing rhythms of crickets." *Physiological entomology* 13.2 (1988): 201-212.
[28] Sprint, M. M., and Eaton, J.L. "Flight behavior of normal and anocellate cabbage loopers (lepidoptera: Noctuidae)." *Annals of the Entomological Society of America* 80.4 (1987): 468-471.
[29] Eaton, J. L., K. R. Tignor, and G. I. Holtzman. "Role of moth ocelli in timing flight initiation at dusk." *Physiological entomology* 8.4 (1983): 371-375.
[30] Wunderer, Hansjörg, and Jacobus Jan De Kramer. "Dorsal ocelli and light-induced diurnal activity patterns in the arctiid moth Creatonotos transiens."*Journal of insect physiology* 35.2 (1989): 87-95.
[31] Land, M. F., and D. E. Nilsson. *Animal Eyes*, New York: Oxford University Press,2002. Hardcover

[32] Kirschfeld, K. "The resolution of lens and compound eyes." *Neural principles in vision*. Springer Berlin Heidelberg, 1976. 354-370.
[33] Krapp, H. G., and Hengstenberg, R. "Estimation of self-motion by optic flow processing in single visual interneurons." *Nature* 384.6608 (1996): 463-466.
[34] Barrows, G. L., Chahl, J. S. and Srinivasan, M.V. "Biomimetic visual sensing and flight control." *Proc. Bristol UAV Conf*. 2002.
[35] Neumann, Titus R., and Heinrich H. Bülthoff. "Insect inspired visual control of translatory flight." *Advances in Artificial Life*. Springer Berlin Heidelberg, 2001. 627-636.
[36] Neumann, Titus R., and Heinrich H. Bülthoff. "Behavior-oriented vision for biomimetic flight control." *Proceedings of the EPSRC/BBSRC international workshop on biologically inspired robotics*. 2002.
[37] Wu, Wei-Chung, et al. "Biomimetic sensor suite for flight control of a micromechanical flying insect: design and experimental results." . *IEEE International Conference on Robotics and Automation, 2003.*
[38] Schenato, Luca, Wei Chung Wu, and Shankar Sastry. "Attitude control for a micromechanical flying insect via sensor output feedback." *Robotics and Automation, IEEE Transactions on* 20.1 (2004): 93-106.
[39] Chahl, Javaan, et al. "Bioinspired engineering of exploration systems: a horizon sensor/attitude reference system based on the dragonfly ocelli for mars exploration applications." *Journal of Robotic Systems* 20.1 (2003): 35-42.
[40] Kerhuel, Lubin, Stéphane Viollet, and Nicolas Franceschini. "Steering by gazing: An efficient biomimetic control strategy for visually guided micro aerial vehicles." *IEEE Transactions on Robotics*, 26.2 (2010): 307-319.
[41] Moore, Richard JD, et al. "A fast and adaptive method for estimating UAV attitude from the visual horizon." *RSJ International Conference on.Intelligent Robots and Systems (IROS), 2011.*
[42] Chahl, Javaan, and Akiko Mizutani. "Biomimetic attitude and orientation sensors." *Sensors Journal, IEEE* 12.2 (2012): 289-297.
[43] Gremillion, Gregory, J. Sean Humbert, and Holger G. Krapp. "Bio-inspired modeling and implementation of the ocelli visual system of flying insects."*Biological cybernetics* 108.6 (2014): 735-746.
[44] Fahle, M., and T. Poggio. "Visual hyperacuity: spatiotemporal interpolation in human vision." *Proceedings of the Royal Society of London B: Biological Sciences* 213.1193 (1981): 451-477.
[45] Adelson, Edward H., and James R. Bergen. "Spatiotemporal energy models for the perception of motion." *JOSA A* 2.2 (1985): 284-299.
[46] Herault, J. *Vision:Images, Signals and Neural Networks*, Progress in Neural Processing Volt.19, World Scientific:Singapore, 2010
[47] Barron, John L., and Neil A. Thacker. "Tutorial: Computing 2D and 3D optical flow." *Imaging Science and Biomedical Engineering Division, Medical School, University of Manchester* (2005).
[48] Lucas, Bruce D., and Kanade, T. "An iterative image registration technique with an application to stereo vision." *IJCAI*. Vol. 81. 1981.
[49] Horn, Berthold K., and Brian G. Schunck. "Determining optical flow." *Technical symposium east*. International Society for Optics and Photonics, 1981.
[50] Stanford Mobile Computer Vision Lecture, Available: http://web.stanford.edu/class/cs231m/lectures/lecture-7-optical-flow.pdf (Last reached 05.06.2016)
[51] Bouguet, Jean-Yves. "Pyramidal implementation of the affine Lucas-Kanade feature tracker description of the algorithm." *Intel Corporation* 5.1-10 (2001): 4.
[52] Farnebäck, Gunnar. "Two-frame motion estimation based on polynomial expansion." *Image analysis*. Springer Berlin Heidelberg, 2003. 363-370.
[53] Smartmotor Developer's Guide Available: http://www.animatics.com/support/download-center.html (Last reached 05.06.2016)
[54] Scheider,K., Conroy, J., Nothwag, W., "Computing Optic Flow with ArduEye Vision Sensor", *U.S. Army Research Laboratory Tech Report*, January 2013.
[55] Krapp, Holger G., Hengstenberg, R., and Egelhaaf, M. "Binocular contributions to optic flow processing in the fly visual system." *Journal of Neurophysiology* 85.2 (2001): 724-734.
[56] Parsons, Matthew M., Krapp Holger G., and Laughlin, Simon B.. "A motion-sensitive neurone responds to signals from the two visual systems of the blowfly, the compound eyes and ocelli." *Journal of Experimental Biology* 209.22 (2006): 4464-4474.
[57] Haag, Juergen, Wertz, and Borst. "Integration of lobula plate output signals by DNOVS1, an identified premotor descending neuron."*The Journal of Neuroscience* 27.8 (2007): 1992-2000.
[58] Parsons, Matthew M., Krapp, Holger G. and Laughlin, Simon B. "Sensor fusion in identified visual interneurons." *Current Biology* 20.7 (2010): 624-628.

[59] Warzecha, Anne-Kathrin, and Egelhaaf, M. "Response latency of a motion-sensitive neuron in the fly visual system: dependence on stimulus parameters and physiological conditions." *Vision research* 40.21 (2000): 2973-2983.
[60] Safran, Moshe N., et al. "Adaptation and information transmission in fly motion detection." *Journal of neurophysiology* 98.6 (2007): 3309-3320.
[61] Vaganay, J., Marie-José Aldon, and A. Fournier. "Mobile robot attitude estimation by fusion of inertial data." *IEEE International Conference on Robotics and Automation, 1993.*
[62] Foxlin, Eric. "Inertial head-tracker sensor fusion by a complementary separate-bias Kalman filter." *Virtual Reality Annual International Symposium, Proceedings of the IEEE, 1996*.
[63] You, Suya, and Ulrich Neumann. "Fusion of vision and gyro tracking for robust augmented reality registration." *Proceedings IEEE Virtual Reality, 2001*.
[64] Wu, Allen D., Eric N. Johnson, and Alison A. Proctor. "Vision-aided inertial navigation for flight control." *Journal of Aerospace Computing, Information, and Communication* 2.9 (2005): 348-360.
[65] Cheviron, Thibault, et al. "Robust nonlinear fusion of inertial and visual data for position, velocity and attitude estimation of UAV." *IEEE International Conference on Robotics and Automation, 2007*
[66] Bleser, Gabriele, and Stricker. "Advanced tracking through efficient image processing and visual–inertial sensor fusion." *Computers & Graphics* 33.1 (2009): 59-72.
[67] Conte, Gianpaolo, and Doherty. "Vision-based unmanned aerial vehicle navigation using geo-referenced information." *EURASIP Journal on Advances in Signal Processing* (2009): 10.
[68] Schall, Gerhard, et al. "Global pose estimation using multi-sensor fusion for outdoor augmented reality." *8th IEEE International Symposium on Mixed and Augmented Reality, 2009.*
[69] Achtelik, Markus, et al. "Onboard IMU and monocular vision based control for MAVs in unknown in-and outdoor environments." *IEEE International Conference on Robotics and Automation (ICRA),* 2011
[70] Campolo, Domenico, et al. "Attitude estimation of a biologically inspired robotic housefly via multimodal sensor fusion." *Advanced Robotics* 23.7-8 (2009): 955-977.
[71] Raspberry Pi Model Summaries Available: https://en.wikipedia.org/wiki/Raspberry_Pi (Last reached 05.06.2016)
[72] Odroid XU4 Summary Available: http://www.hardkernel.com/main/products/prdt_info.php?g_code=G143452239825 (Last reached 05.06.2016)
[73] Menzel, Randolf. "Spectral sensitivity and color vision in invertebrates."*Comparative physiology and evolution of vision in invertebrates*. Springer Berlin Heidelberg, 1979. 503-580.
[74] Hori, Masatoshi, et al. "Lethal effects of short-wavelength visible light on insects." *Scientific reports* 4 (2014).
[75] Shimoda, Masami, and Ken-ichiro Honda. "Insect reactions to light and its applications to pest management." *Applied Entomology and Zoology* 48.4 (2013): 413-421.
[76] Virsik, Renata P., and W. Reichardt. "Detection and tracking of moving objects by the fly Musca domestica." *Biological Cybernetics* 23.2 (1976): 83-98.
[77] Reichardt, Werner, and Tomaso Poggio. "Figure-ground discrimination by relative movement in the visual system of the fly, Part I: Experimental Results" *Biological Cybernetics* 35.2 (1979): 81-100.
[78] Reichardt, Werner, Tomaso Poggio, and Klaus Hausen. "Figure-ground discrimination by relative movement in the visual system of the fly, Part II: Towards the Neural Circuitry." *Biological Cybernetics* 46.1 (1983): 1-30.
[79] Egelhaaf, M. "On the neuronal basis of figure-ground discrimination by relative motion in the visual system of the fly. 1: Behavioural constraints imposed on the neuronal network and the role of the optomotor system." *Biological Cybernetics* 52.2 (1985).
[80] Stone, T., et al. "Sky segmentation with ultraviolet images can be used for navigation." *Proceedings Robotics: Science and Systems*. 2014.
[81] Kollmeier, Thomas, et al. "Spectral contrasts for landmark navigation."*JOSA A* 24.1 (2007): 1-10.
[82] Tehrani, Mohsen H., Garratt, M.A, and Anavatti, S. "Horizon-based attitude estimation from a panoramic vision sensor." *Embedded Guidance, Navigation and Control in Aerospace*. Vol. 1. No. 1. 2012.
[83] Shabayek, Abd El Rahman, et al. "Vision based uav attitude estimation: Progress and insights." *Journal of Intelligent & Robotic Systems* 65.1-4 (2012): 295-308.
[84] Cornall, T. D., Egan, G., and Price, A. "Aircraft attitude estimation from horizon video." *Electronics Letters* 42.13 (2006): 744-745.
[85] Mondragón, Iván F., et al. "Omnidirectional vision applied to Unmanned Aerial Vehicles (UAVs) attitude and heading estimation." *Robotics and Autonomous Systems* 58.6 (2010): 809-819.
[86] Thurrowgood, Saul, et al. "A vision based system for attitude estimation of UAVs." *Intelligent Robots and Systems, 2009. IROS 2009. IEEE/RSJ International Conference on*. IEEE, 2009.

[87] Taylor, Brian, et al. "Horizon sensing attitude stabilisation: A VMC autopilot."*18th International UAV Systems Conference*, 2003.
[88] Collett, T. S., and J. Zeil. "The selection and use of landmarks by insects." *Orientation and communication in arthropods*. Birkhäuser Basel, 1997. 41-65.
[89] HOYA U340 Filter Specifications Available: http://www.hoyaoptics.com/pdf/U340.pdf (Last reached 05.06.2016)
[90] GUVA-S12 Datasheet Available: https://cdn-shop.adafruit.com/datasheets/1918guva.pdf (Last reached 05.06.2016)
[91] TSL14S Light-to-Voltage Converter Datasheet Available: http://www.mouser.com/ds/2/588/TSL14_Datasheet_EN_v1-540303.pdf (Last reached 05.11.2016)
[92] Coherence (Signal Processing) Available: https://en.wikipedia.org/wiki/Coherence_(signal_processing) (Last reached 05.12.2016)